

THREE-DIMENSIONAL RECONSTRUCTION METHODS FOR MICRO-ROTATION FLUORESCENCE MICROSCOPY

Danai Laksameethanasan



TEKNILLINEN KORKEAKOULU
TEKNISKA HÖGSKOLAN
HELSINKI UNIVERSITY OF TECHNOLOGY
TECHNISCHE UNIVERSITÄT HELSINKI
UNIVERSITE DE TECHNOLOGIE D'HELSINKI

THREE-DIMENSIONAL RECONSTRUCTION METHODS FOR MICRO-ROTATION FLUORESCENCE MICROSCOPY

Danai Laksameethanasan

Dissertation for the degree of Doctor of Science in Technology to be presented with due permission of the Faculty of Information and Natural Sciences, for public examination and debate in Room As1, Tuus building at Helsinki University of Technology (Espoo, Finland) on the 27th, February 2009, at 12.00 noon.

Helsinki University of Technology
Department of Electrical and Communications Engineering
Laboratory of Computational Engineering

Teknillinen korkeakoulu
Sähkö- ja tietoliikennetekniikan osasto
Laskennallisen tekniikan laboratorio

Helsinki University of Technology
Department of Biomedical Engineering and Computational Science
P.O. Box 9203
FIN-02015 TKK
FINLAND
Tel. +358 9 451 4826
Fax. +358 9 451 4830
<http://www.becs.tkk.fi>

Online in PDF format: <http://lib.tkk.fi/Diss/2009/isbn9789512297559/>

E-mail: danai.laksameethanasan@tkk.fi

© Danai Laksameethanasan

ISBN 978-951-22-9754-2 (printed)

ISBN 978-951-22-9755-9 (PDF)

ISSN 1797-3996

Picaset Oy

Helsinki, Finland 2009

Abstract

Micro-rotation fluorescence microscopy is a novel, optical imaging technique developed with a cell rotation system. The imaging system enables individual living cells to be rotated in suspension under microscopic dimensions, and allows us to acquire a series of images of the cells, simultaneously during the rotation. A challenging task in micro-rotation imaging is how to determine three-dimensional (3D) cell structure from the image series.

This thesis thus presents four alternative methods for reconstructing 3D objects from a series of micro-rotation images. The three former methods, the expectation maximisation (EM), the generalised Skilling-Bryan and the marginalisation methods, are iterative algorithms built on the Bayesian inversion theory, which is used to quantify uncertainties in data and model parameters, and also to utilise prior information about the unknown structure. The fourth method, dual filtered backprojection (DFBP), is a fast, non-iterative algorithm derived from the Fourier slice theorem in the classical computed tomography. Each method has its own features: the EM method serves as a basic tool for general usability; the Skilling-Bryan method is more flexible for modelling of noise and prior; the marginalisation method serves as a statistical treatment of the reconstruction that suffers from inaccurate image alignment; and the DFBP method beats the other methods by computational speed but restricts itself with a certain imaging condition. In general, selection of the reconstruction methods depends on imaging and data conditions, such as conventional widefield or confocal microscopy, the stability of cell rotation, and the quality of image alignment.

In conclusion, all the proposed reconstruction methods clearly increase capability to visualise 3D object structures, as shown by both simulations and experiments with real micro-rotation data. Two obvious messages from the results are that first, the quality of the reconstructed object highly depends on the accuracy of image alignment, and second, micro-rotation reconstructions with the current imaging system always contain poor resolution in the tangential direction of the rotation. Future interesting research is thus to combine the micro-rotation protocol with extended depth-of-focus microscopy that could strengthen the tangential resolution.

Keywords: optical microscopy, micro-rotation imaging, deconvolution, tomography, image reconstruction, statistical inverse problems, cell biology.

Preface

This thesis is the result of my research in the Department of Biomedical Engineering and Computational Science, Helsinki University of Technology during the years 2005 to 2008. This work was supported by the European Commission (FP6 NEST program; the project AUTOMATION; contract number 4803).

I am grateful to Prof. Kimmo Kaski and Prof. Jouko Lampinen for providing me the opportunity to conduct my research interest and the excellent environment to complete this work. I deeply thank Dr. Sami S. Brandt, my research supervisor, for numerous discussions and fruitful suggestions. While he has been busy with his own work, he always had time for a talk and it has been enjoyable to work with him. My special thanks also goes to Dr. Peter Engelhardt and Dr. Jukka Heikkonen, who gave me many insightful suggestions. I would like to thank all my collaborators, Dr. Olivier Renaud and Dr. Spencer Shorte at Institut Pasteur, Paris, for helpful discussions and providing all the image data. I additionally thank all collaborators in the AUTOMATION consortium.

I have enjoyed and benefited from many lively discussions with all my colleagues in our research group, Dr. Vibhor Kumar, Kimmo Palander, Tapio Nieminen, Pentti Jääskeläinen, Tommi Tykkälä and Markos Mevorah. I am thankful to Eeva Lampinen, Kaija Virolainen and Senja Kojonen, for patiently taking care of many practical issues that come up throughout the years.

Finally, I wish to thank my family, mother Siriya, farther Chirdsak, grandmother Sui-Ngo, brother Montri, and my girl Pao, for supporting me with their relaxing talks during these years. I would like also to thank all my friends in Finland for helping me to maintain a life outside this work.

Espoo, 10th February 2009

Danai Laksameethanasan

List of Publications

1. Danai Laksameethanasan, Sami S. Brandt and Peter Engelhardt (2006). A Three-Dimensional Bayesian Reconstruction Method with the Point Spread Function for Micro-Rotation Sequences in Wide-Field Microscopy. In Proc. IEEE International Symposium on Biomedical Imaging (*ISBI 2006*), pp. 1276–1279, Arlington, VA, April 2006.
2. Danai Laksameethanasan and Sami S. Brandt (2007). Generalised Skilling–Bryan Minimisation for Micro-Rotation Imaging in Light Microscopy. AIP Conf. Proc.: 27th International Workshop on Bayesian Inference and Maximum Entropy Methods (*MaxEnt2007*), Vol. 954 pp. 354–361, Saratoga Springs, New York, July 2007.
3. Danai Laksameethanasan, Sami S. Brandt, Peter Engelhardt, Olivier Renaud, and Spencer L. Shorte (2008). A Bayesian Reconstruction Method for Micro-Rotation Imaging in Light Microscopy. *Microscopy Research and Technique*, 71(2), 158–167.
4. Danai Laksameethanasan and Sami S. Brandt (2009). A Bayesian Reconstruction Method with Marginalised Uncertainty Model for Camera Motion in Micro-Rotation Fluorescence Microscopy¹. *IEEE Transaction on Biomedical Engineering*, Submitted.
5. Danai Laksameethanasan, Sami S. Brandt, Olivier Renaud, and Spencer L. Shorte (2009). Dual Filtered Backprojection for Micro-Rotation Confocal Microscopy. *Inverse Problems*, 25(1), 015006.

¹*Helsinki University of Technology, Department of Biomedical Engineering and Computational Science*, Technical report A08, ISBN 978-951-22-9756-6.

Author's Contribution

The research is a result of collaboration between the author of this thesis and the other authors in the described publications. The author of the thesis has implemented all computer programs used in the publications and has analysed their results with the other described authors. As the primary author of all publications, the thesis's author is responsible for their written material. The real micro-rotation images used in the publications were acquired by Olivier Renaud, Christophe Machu, and Spencer Shorte (Institut Pasteur, Paris). The point spread functions and the 3D cell phantom used in the publications were obtained from Scientific Volume Imaging (<http://www.svi.nl>).

Contents

Abstract	1
Preface	3
List of Publications	5
Author's Contribution	7
1 Introduction	11
1.1 Research Background	11
1.2 Research Problems	12
1.3 Research Aims	13
2 Fluorescence Microscopy	15
2.1 Fluorescence Microscope Systems	15
2.2 Image Formation Models	21
3 Reconstruction Methods	25
3.1 Statistical Methods	26
3.1.1 Optimisation: Generalised Skilling-Bryan Method	30
3.1.2 Expectation Maximisation Method	32
3.1.3 Reconstruction with Motion Uncertainty Model	35
3.2 Fourier Method	39
3.3 Summary and Examples	42
4 Results and Method Assessments	45
5 Conclusions and Discussion	50
Bibliography	51

Chapter 1

Introduction

1.1 Research Background

Three-dimensional (3D) fluorescence imaging of non-adherent living cells is an essential tool in cell biology and biomedical science for analysing their metabolic functions. In 3D imaging, understanding of optical and geometric characteristics plays an important role: how to effectively collect a 2D image series in order to recover spatial information inside the specimen. To date, most of 3D fluorescence imaging techniques use the conventional *through-stacking* protocol to acquire a 3D image stack by shifting either the focal plane of microscope objective or biological samples along the optical z -axis (Agard et al. 1989, McNally et al. 1999). The fundamental limitation in through-stack imaging is that the axial (z) resolution is always several folds weaker than the lateral (xy) resolution. The through-stacking protocol compounds this problem such that any resulting 3D reconstruction is distorted by the x, y, z resolution asymmetry, and the surface and volume of objects are convolved in a complex manner. Another crucial limitation to the through-stacking technique, particularly for 3D imaging of living cells, is that samples need to be stabilised during image acquisition and often done by firmly attaching the samples on a hard surface (cover glass). The stabilisation by the attachment can change the original 3D shape of the cells in a way that effects their native functions (Lee et al. 2004, Kang et al. 2007).

Micro-rotation fluorescence microscopy has been developed to overcome such limitations by using dielectric field cage (DFC) technology, that has been demonstrated as a useful tool for non-tactile manipulation of living cells in suspension (Schnelle et al. 1993, Fuhr et al. 1994). The principle of DFC involves organising the intensity and phase difference between eight electrodes to create a 3D dielectric cage for cell trapping and to produce rotational force for the cell rotation (Figure 1.1). In micro-rotation imaging, rather than shifting the focal plane, dielectric fields trap non-adherent cells in suspension inside the 3D electrode cage and continuously rotate them fully 360 degrees approximately around a chosen axis, parallel to the fixed focal plane (Shorte et al. 2003). During the continuous

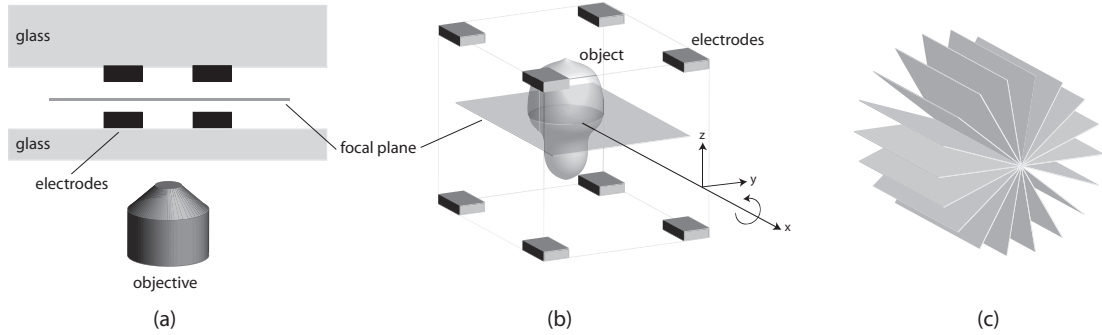


Figure 1.1: Schematic illustration of micro-rotation imaging. (a) dielectric field channel with eight electrode strips: four attached on the top glass and four on the bottom glass; (b) 3D electrode cage with the eight electrodes with an object, being rotated (by the controlled electric fields) around a single axis parallel to the focal plane; (c) micro-rotation imaging geometry where each plane represents the position of focal plane in the object coordinate frame.

rotation, the cells are sequentially imaged by an optical microscope, and usually fluorescence microscope. An image example from real micro-rotation series is shown in Figure 1.2. The advantage of the micro-rotation technique is that it offers unique possibility to visualise non-adherent live cells from any orientations in native environment that provides a way for improving 3D optical resolution, particularly along the z -axis (Lizundia et al. 2005, Korlach et al. 2005). Today, a major challenge in micro-rotation imaging is to develop powerful, computational methods for reconstructing 3D object structures from a series of micro-rotation images.

1.2 Research Problems

Reconstruction of 3D objects from multiple projection images is an inverse problem, which has been intensively developed in the past decades. Inverse problem is a task to find unknown physical quantities (parameters or object intensities) that cannot be observed from direct measurement; these parameters need to be estimated from observable quantities, such as measurement data or projection images. A common feature of inverse problem is its ill-posedness, i.e. small noise in the observed data or small errors in the model may produce huge perturbations in estimation of the parameters. The usual treatment for the ill-posedness can be categorised into two major groups: the classical inversion and the statistical inversion (Calvetti & Somersalo 2007). The classical inversion is built on the linear algebra theory and often concerned with the questions about existence, uniqueness and stability of the solution. The resulting uniqueness and stability are helpful for analysing the obtained solutions as well as what information is required in addition to the actual measurement. On the other hand, the statis-

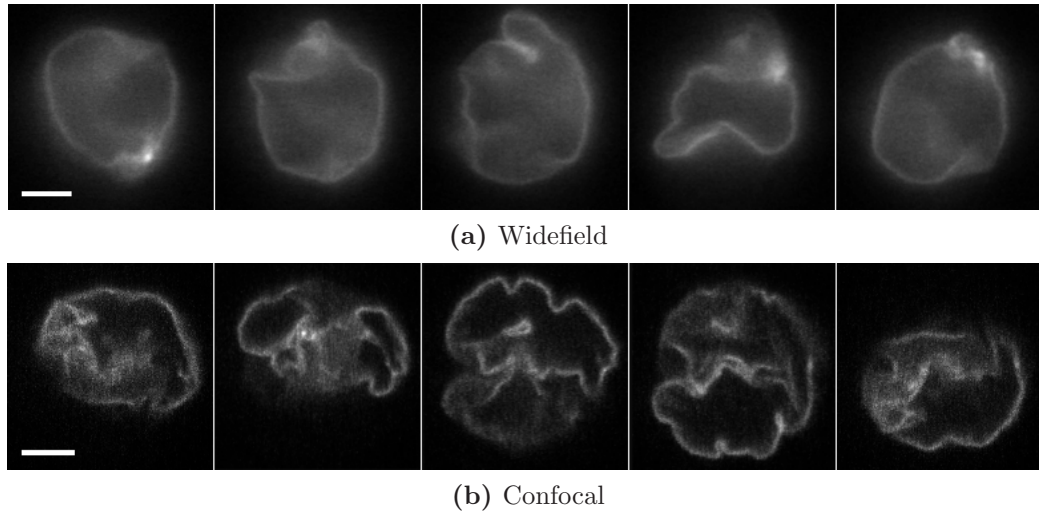


Figure 1.2: Five image example from two series of real micro-rotation images acquired using (a) widefield microscope and (b) confocal microscope. Each image series represents the nuclear membrane of a single human living cell expressed by green fluorescent protein (GFP) markers. Scale bars indicate $5 \mu\text{m}$.

tical inversion formulates inverse problems based on the Bayesian principle that provides valid utilisation of prior information and data uncertainty (Kaipio & Somersalo 2004). An alternative advantage of the Bayesian method in addition to the use of prior information, is the possibility to evaluate the reliability in the estimated solutions. According to these features, the main focus of this thesis is oriented towards the Bayesian inversion approach.

Determining actual object from multiple images often requires preknowledge about projection directions, or motion parameters that describe the orientation of the object. The reconstruction problem therefore involves not only object density recovery to reconstruct the actual object, but also motion estimation to determine the object orientation. This thesis, however, considers only the problem of object recovery and assumes that the motion parameters are available. In the context of the thesis, the problem of motion estimation has been addressed to a large extent in Palander (2007) and Yu et al. (2008).

1.3 Research Aims

The primary goal of this thesis is to develop appropriated reconstruction algorithms for micro-rotation imaging, and to study imaging characteristics of the novel micro-rotation system. The secondary objective is to gain new scientific knowledge that can be applied into related imaging applications in the field of inverse problems.

The thesis is organised as follows. Chapter 2 presents an overview of fluo-

rescence microscopy that includes standard and modern high-resolution optical techniques, and also introduces the through-stack and the micro-rotation imaging protocols together with their image formation models. The aim of Chapter 3 is to describe theoretical concepts behind the statistical reconstruction methods and the Fourier-based method used in the Publications. In Chapter 4, results and assessment of the proposed reconstruction methods are presented based on the Publications. Finally, we conclude and discuss the thesis in Chapter 5.

Chapter 2

Fluorescence Microscopy

Ability to image interior structures of living cells in three dimensions is an integral part of understanding how the cells work. Visualisation of the interior of *living cells* is, however, beyond the potential of electron microscopy and optical near-field microscopy due to the restricted requirement for fixed sample preparations (Engelhardt 2000) and surface-bound imaging (Novotny & Hecht 2006). Optical microscopy, particularly fluorescence microscopy, is still very widely used in biological sciences, due to its unique capability to reveal interior cell organelles and allow subcellular localisation in living cell preparations. Although the classical resolution of optical microscopy is limited by about half of the wavelength of light (diffraction limit), modern optical techniques (Hell 2009) have demonstrated to provide resolution beyond the diffraction limit, that reduces the resolution gap between optical and electron microscopy.

The aim of this chapter is to present the basis of fluorescence microscopy including the widefield and confocal microscopes, and also shortly describe other high-resolution techniques in optical microscopy. We then introduce through-stack and micro-rotation imaging together with their image formation models.

2.1 Fluorescence Microscope Systems

The fluorescence microscope is an optical microscope used to study and to visualise the interior of cells and organisms using the fluorescence technique (Murphy 2001). In fluorescence microscopy, the sample labelled with a fluorescent molecule, a fluorophore, is illuminated by the excitation light; the fluorophores in the sample then release emission light, which is transmitted through objectives and focused to the detector (eyes or camera) to produce an image (Figure 2.1). The unique advantage of fluorescence imaging is its ability to image specific organelles in a living cell using multicolour molecular labelling, where this feature is not shared by high-resolution techniques such as electron microscopy (Frank 2006) and scanning-probe techniques (Novotny & Hecht 2006). Despite the attractive feature in multicolor live imaging, fluorescence microscopy consists

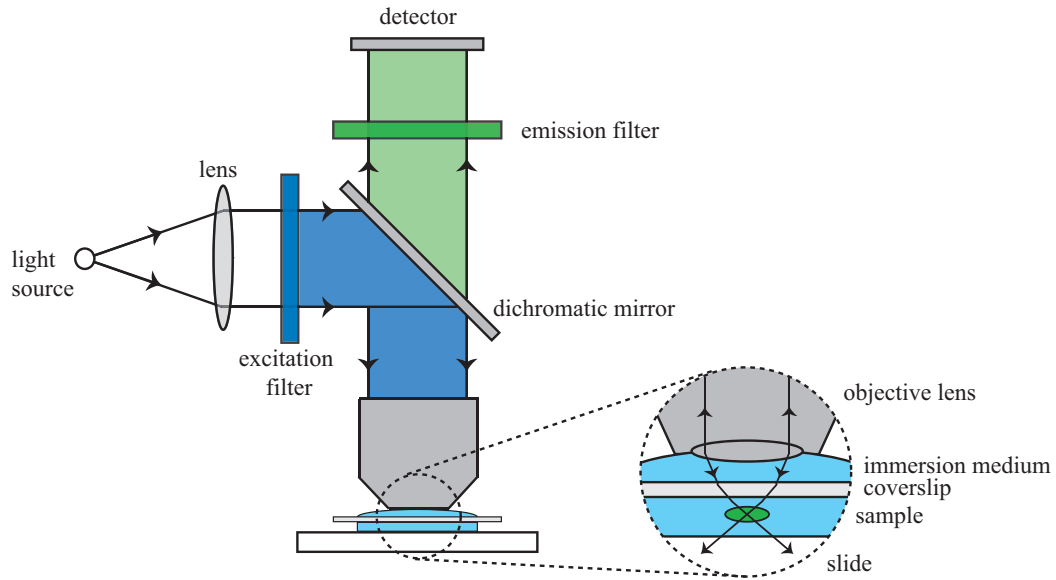


Figure 2.1: Principle of (epi-) fluorescence microscope. The excitation light with certain wavelength (blue) from the light source passes through the excitation filter, reflects at the dichromatic mirror, and illuminates on the sample through the objective lens. The emission light with longer wavelengths (green) from the sample reflects back and passes through the dichromatic mirror and the emission filter to the detector (eye or camera).

of two usual limitations: the first is the diffraction limit in ordinary optical microscopy where its spatial resolution is bounded by the wavelength of light; and the second relates to the fluorescence phenomena, photobleaching and phototoxicity, where the fluorophores or the living cells itself are gradually destroyed during the light illumination.

Widefield and Confocal Microscopy

Fluorescence microscopes can be categorised into two major groups: widefield and confocal microscopes. The widefield microscope is the most common type of microscope in fluorescence imaging. In conventional widefield imaging, the complete sample is uniformly illuminated by the excitation light and the light emitted from the entire sample is simultaneously recorded on the detector (Figure 2.2a). A widefield image therefore contains not only in-focus information from on the focal plane, but also out-of-focus light from other sections nearby the focal plane. The out-of-focus light is a source of blur in widefield images (Figure 1.2a) that can be removed either computationally by deconvolution methods (Biggs 2004) or physically by the use of confocal pinhole to block the out-of-focus light.

Confocal microscopes are thus designed to eliminate the out-of-focus light

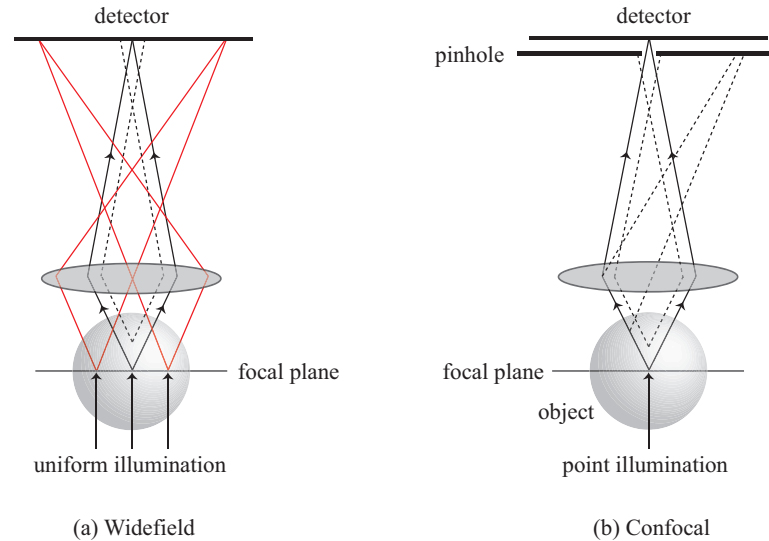


Figure 2.2: Principle of (a) widefield microscope and (b) confocal microscope. (a) A large volume of the sample is uniformly and simultaneously illuminated by excitation light. The light, emitted from the focal plane (in-focus light; solid line) and from other planes nearby (out-of-focus light; dash line), is recorded on the detector as an image. (b) Only a small volume of the sample (or a small point of the focal plane) is illuminated by excitation light (laser source). Only the in-focus light (solid) emitted from the focal plane is recorded by the detector, whereas most of the out-of-focus light (dash) emitted at positions above and below the focal plane is blocked by the detection pinhole. A confocal image therefore contains mainly the sample information located on the focal plane.

reaching the detector using a pinhole (Pawley 2006). The first confocal microscope type is *laser scanning confocal* microscope. Rather than entirely illuminating the sample, only small volume in the sample is illuminated by the laser point source and therefore the sample must be scanned to form a complete image (Figure 2.2b). Although the capability in rejecting the out-of-focus light provides a clearer and sharper details in images (Figure 1.2b), the required raster scanning substantially slows down image acquisition rates. The *spinning-disk confocal* microscopes have hence been developed to improve the acquisition speed in laser scanning. Instead of illuminating excitation light through a single confocal pinhole, the spinning-disk technique uses a disc with a series of pinholes to simultaneously illuminate many points on the sample. The arrangement of the pinholes on the disk is such that as when the disk rotates, the illumination spot scan the entire plane to form an image. Perhaps one of the most important drawbacks for the both types of confocal microscope is that, when working with the weak fluorescence intensities of biological samples, the pinhole diameter has to be increased beyond its ideal size, which reduces the resolution of the confocal microscope.

Point Spread Function

The imaging properties of a fluorescence microscope either widefield or confocal types can be described by its point spread function (PSF)—a representation of a 3D diffraction pattern (images) of light that is emitted from a single point source in the specimen and transmitted to the detector through microscope objectives. The PSF of a microscope can be estimated either theoretically or from a direct measurement. The experimental PSF can be measured as a 3D image of a small point-like object such as a fluorescent bead (usually smaller than 200 nm). The image quality of the experimental PSF is usually worse due to the presence of high-frequency noise and therefore, the average of 3D images from many individual fluorescent beads often used to improve the PSF quality, instead from a single bead.

The theoretical PSF is derived from the diffraction theory of light (Born & Wolf 1999, Goodman 2005) and often depends on imaging parameters such as the numerical aperture of objective, the excitation and emission wavelengths, and the refractive index of the immersion medium (van der Voort & Brakenhoff 1990, Gibson & Lanni 1991). Figure 2.3 (a–b) shows an example of theoretical PSFs of widefield and confocal microscopes. The PSF can be used to measure the maximum resolved resolution of the microscope, which describes its ability to distinguish two point objects in an image, or equivalently minimum distance between distinguishable objects. In general, the microscope resolution is determined by the main width of PSF, often defined by its full width at half maximum (FWHM) in the direction of interest. The FWHM of the PSF depends on the wavelength of light λ and the numerical aperture ($\text{NA} = n \sin \theta$), which is proportional to the refractive index n of the sample-embedded medium and half of the maximum open angle θ of light beams collected by the microscope objective.

Various definitions of the resolution measure exist in the literature (den Dekker & van den Bos 1997). The classical approach to measure the resolution of the conventional widefield microscope is the *Rayleigh criterion*, which is the distance from the central maximum to the first minimum of the PSF profile. Mathematically, it is given by

$$R_{xy} = \frac{0.61\lambda}{\text{NA}}, \quad R_z = \frac{2n\lambda}{\text{NA}^2}, \quad (2.1)$$

where R_{xy} and R_z are the minimum resolved distance in the lateral and the axial directions. Another well-known approach is to consider the *frequency support* (non-zero values) of the spectrum of PSF, or the optical transfer function (OTF) (Figure 2.3c,d). This is because a fluorescence image is a convolution of the object with the PSF in real space and, by the convolution theorem, the image spectrum is the pointwise product between the object spectrum and the OTF. Therefore, a microscope cannot detect high-frequency information in the object that locates outside the OTF support.

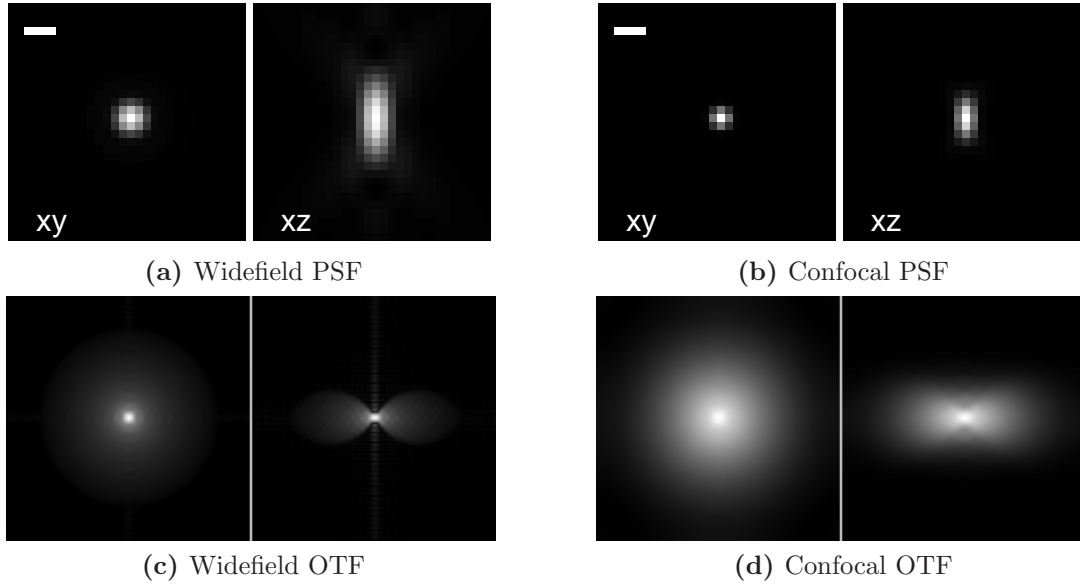


Figure 2.3: Theoretical point spread function (PSF) of (a) widefield microscope and (b) confocal microscope. Each PSF displays lateral (xy) and axial (xz) planes at the centre of the PSF. (c) and (d) presents the corresponding optical transfer functions (OTF) of the widefield and the confocal microscope, respectively. The theoretical PSFs were computed using the SVI Huygens softwareTM where its implementation is based on the vector diffraction theory. The microscope parameters used are $63\times$ water-immersion objective, numerical aperture 1.2, excitation wavelength 488 nm and emission wavelength 520 nm. Scale bars indicate $0.5\ \mu\text{m}$.

Three-Dimensional Imaging

3D fluorescence imaging of living organisms has become popular in biomedical science during the preceding decades. A reason for the popularity is that the interpretation of imaging results in 3D truly shows what happens within, e.g., living cells (Abbott 2003, Webb & Horwitz 2003). To achieve 3D imaging, most of commercialized imaging microscopes use so-called *axial through-stack* (z -stack) protocol, or optical sectioning technique (Agard et al. 1989, McNally et al. 1999). This technique requires that samples are stabilized by attachment to a cover glass and, to collect a through-stack of 2D images, the focal plane of the microscope is shifted in small steps along the optical (z) axis (Figure 2.4a). It is well known that in through-stack imaging with both widefield and confocal microscopes, the resolution along the z -axis is much less than the resolution in the xy -plane. This bounded resolution in the axial direction provides a significant limit in the 3D analysis of biological structures with the size comparable to the resolution of the microscope. Improving the axial resolution, or equivalently achieving 3D symmetric resolution, is therefore one of the most studied research topic in 3D optical imaging.

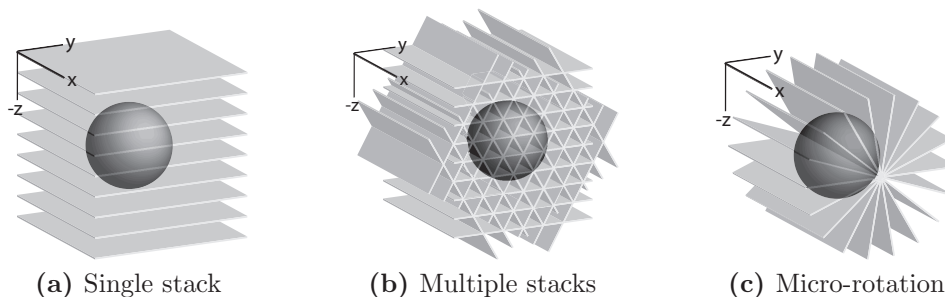


Figure 2.4: Data acquisition geometries in 3D fluorescence imaging. (a) Through (single) stack; (b) Multiple stacks with three orientations; (c) Micro-rotation. Each plane represents the focal plane in the object coordinate frame.

In the last decade, numerous high-resolution techniques have been developed to improve the axial resolution as well as the lateral resolution (Gustafsson 1999, Török & Kao 2003, Hell 2009). Most of the high-resolution techniques rely on similar principle: fluorescence molecules are switched on and off sequentially in time, to avoid interference between adjacent objects. *4Pi* microscopy (Hell & Stelzer 1992) uses two objective lenses to simultaneously illuminate the sample from two orthogonal directions, and the resulting superposition pattern makes the PSF with an increased axial resolution. *Two-photon* microscopy (Zipfel et al. 2003) uses two-photon absorption to excite the sample: the probability of a fluorescence photon to be emitted increases quadratically with the excitation intensity, meaning that the excitation PSF is the square of the widefield PSF resulting the narrower main-width of the PSF. *Structured illumination* microscopy (Gustafsson et al. 2008) uses a diffraction grating to split excitation light into different light patterns, which are used to excite the sample. The sample then generates emission light that contains high-frequency information (which is shifted in frequency space) used to produce high-resolution images. All the techniques above however restrict to 3D imaging with the single through-stack protocol and, therefore, the axial resolution remains worse than the resolution in lateral direction.

An alternative family of high-resolution techniques that attempt to overcome resolution asymmetry is multiple through-stack microscopy, or axial tomographic microscopy (Shaw et al. 1989, Cogswell et al. 1996, Bradl et al. 1996, Heintzmann & Cremer 2002). Its key idea is straightforward: several image stacks are acquired in different orientations by rotating the sample or using multiple lenses oriented around the sample of interest (Huisken et al. 2007). The multiple stacks are then fused into a single reconstruction volume (Figure 2.4b) using a computational method (see Heintzmann & Cremer 2002). This technique significantly enhances the axial resolution while the lateral resolution slightly degrades, comparing to the reconstruction using the conventional single stack. Two major difficulties in multiple stack imaging are that this approach requires accurate stack alignment,

and complex data acquisition which requires *non-simultaneous* recording of the oriented volumes.

Micro-Rotation Imaging

Micro-rotation cell imaging has thus been developed with the dielectric field cage (DFC) technology to overcome these two limits: the poor axial resolution and the sample stabilisation by surface attachment. The principle of DFC technology involves modulating the electric current at each electrode to create dielectric fields in such a way that allows an individual cell to be manipulated and rotated in microscopic dimensions under an optical microscope (Schnelle et al. 1993, Schnelle et al. 2000, Shorte et al. 2003). The interactions between dielectric fields and the cell depend on the dielectric structure of the cells, the conductance and dielectric constant of the suspended medium, as well as the applied frequency and voltage of electric current to the electrodes (usually ranging in order of hundred kHz and Volts). Furthermore, living cells tend to do not suffer from any biological damage with the manipulation in this manner, making the DFC technology attractive for 3D live cell imaging. In micro-rotation imaging, while the cell continuously rotates around a chosen axis parallel to the focal plane, images of the rotating cell are sequentially recorded using various optical imaging modalities, for instance, conventional wide-field microscopy, laser-scanning or spinning-disk confocal microscopy. In contrast to single and multiple through-stack imaging, only a single 2D image is taken from each direction, as illustrated in Figure 2.4c.

In addition to micro-rotation geometry, the DFG technology can be applied for multiple through-stacking imaging by performing stepwise rotation of object, instead of continuous rotation, together with shifting the focal plane to collect each through stack. The advantage of this approach includes not only the ability to improve the 3D resolution but also to handle 3D imaging of non-adherent cells. The drawback of the DFG multiple through-stacking, however, remains the same as the conventional multiple through-stacking, that is, it gives low speed in image acquisition that can be problematic for live cell imaging. The use of the DFG technology with the multiple through-stacking protocol has been addressed in a large context by Renaud et al. (2008).

The rest of this chapter describes image formation of through-stack and micro-rotation imaging, based on the concept of PSF. The image formation models will be used as a basis for the reconstruction algorithms in the next chapter.

2.2 Image Formation Models

Conventional Through-Stack

Within the linear shift-invariance system, the 3D measurement volume in through-stack imaging can be represented by a convolution between the 3D PSF of the

microscope and the 3D object of interest. Mathematically, the convolution operation is written as

$$\begin{aligned} g(x, y, z) &= \iiint h(x - x', y - y', z - z') f(x', y', z') dx' dy' dz', \\ &= h(x, y, z) * f(x, y, z), \end{aligned} \quad (2.2)$$

where f is the piecewise-continuous object volume evaluated at the position (x, y, z) , g is the piecewise-continuous measurement volume, h is the 3D PSF and $*$ denotes the 3D convolution operator. That is, the 3D image is represented a sum of the collection of PSFs where their positions and intensities are adjusted according to the corresponding point sources in the sample.

The discretised model for (2.2) can be represented as a matrix form

$$\mathbf{g} = \mathbf{H}\mathbf{f} \quad (2.3)$$

where $\mathbf{g} \in \mathbb{R}^N$ is a vector of 3D image data, $\mathbf{f} \in \mathbb{R}^N$ is a vector of object densities (N voxels) and $\mathbf{H} \in \mathbb{R}^{N \times N}$ is the Toeplitz matrix representing the 3D convolution operations with the PSF. In practice, the matrix-vector product between \mathbf{H} and \mathbf{f} can be efficiently implemented using the fast Fourier transform (FFT) algorithm.

Micro-Rotation

In micro-rotation imaging, a series of images is simultaneously acquired while the object is continuously rotated around a single axis parallel to the focal plane of microscope objective. Assuming linear shift-invariance, a measurement image m_i obtained at the projection direction i is represented by

$$m_i(x, y) = A_{\theta_i} f(x, y, z) = P\{h(x, y, z) * R_{\theta_i} f(x, y, z)\}, \quad (2.4)$$

where A_{θ_i} is the linear operator describing the image formation model, R_{θ_i} is the rotation-translation operator defined as a function of the motion parameters θ_i and P is the ideal *slicing* operator that picks up a single plane corresponding to the focal plane. The 3D convolution in (2.4) can be efficiently computed using 2D convolution between the object and PSF slices which are parallel to the focal plane, and thereafter all the convoluted 2D slices are summed along the z -axis to obtain the measurement image m_i (see Publication 3).

The discretised model of (2.4) can be represented as a linear system

$$\mathbf{m}_i = \mathbf{A}_{\theta_i} \mathbf{f} = \mathbf{P} \mathbf{H} \mathbf{R}_{\theta_i} \mathbf{f}, \quad (2.5)$$

where $\mathbf{m}_i \in \mathbb{R}^M$ is a vector of image densities (M pixels) for the projection i , $\mathbf{f} \in \mathbb{R}^N$ is a vector of object densities (N voxels), $\mathbf{A}_{\theta_i} \in \mathbb{R}^{M \times N}$ is a projection matrix, \mathbf{P} is a projection matrix which picks the object plane coinciding with the focal plane, \mathbf{H} is the Toeplitz matrix representing the 3D convolution opera-

tions, and $\mathbf{R}_{\theta_i} \in \mathbb{R}^{N \times N}$ is the rotation-translation matrix defined by six motion parameters $\theta_i = (\alpha_i, \beta_i, \gamma_i, t_{x_i}, t_{y_i}, t_{z_i})$. The first three parameters are rotation angles (α, β, γ) describing the 3D orientation of object¹ and the rest are translation parameters (t_x, t_y, t_z) that indicate the position of the object with respect to the centre of the focal plane. In practice, the matrix-vector product $\mathbf{R}_{\theta_i} \mathbf{f}$ is computed by the rigid transformation operating on the 3D object coordinate with the six motion parameters, and thereafter we apply the linear interpolation for determining intensity values located in between 3D grid points. The matrix-vector product between the Toeplitz matrix \mathbf{H} and the rotated object $\mathbf{R}_i \mathbf{f}$ can be efficiently computed using the fast Fourier transform algorithm. In the optimisation problem, we additionally need the adjoint operator of A_{θ_i} , or equivalently the transpose matrix $\mathbf{A}_{\theta_i}^T = \mathbf{R}_{\theta_i}^T \mathbf{H}^T \mathbf{P}^T$ which involves zero-padding, correlation with the PSF and rotation of the volume. The derivation and implementation of the adjoint operator have been addressed in detail in Publication 3.

In estimating the reconstruction, we solve the equation (2.4) simultaneously for all the projections. The total linear model composed from (2.5) is given by

$$\mathbf{m} = \mathbf{A}_{\theta} \mathbf{f}, \quad (2.6)$$

where $\mathbf{m} = [\mathbf{m}_1^T, \dots, \mathbf{m}_K^T]^T \in \mathbb{R}^{KM}$ is a joint vector of the K image vectors, $\mathbf{A}_{\theta} = [\mathbf{A}_{\theta_1}^T, \dots, \mathbf{A}_{\theta_K}^T]^T \in \mathbb{R}^{KM \times N}$ is a joint projection matrix including the K projection matrices, and $\theta = [\theta_1^T, \dots, \theta_K^T]^T \in \mathbb{R}^{6K}$ is a joint vector of motion parameters. The similar model that solves the deconvolution problem with multiple projection images has been also proposed in fluorescence microscopy and astronomy (see, for instance, Verveer & Jovin 1999, Heintzmann & Cremer 2002, Anconelli et al. 2006).

Deconvolution Algorithms: A Short Survey

Determining the unknown object \mathbf{f} from a set of micro-rotation images \mathbf{m} in (2.6) is related to solve \mathbf{f} in the through-stack model (2.3), which is a well-known deconvolution problem, or the image restoration problem. According to the relationship between these two imaging techniques, we now give a short survey in deconvolution algorithms applied to through-stack imaging, and thereafter introduce the reconstruction algorithms for micro-rotation imaging in the next chapter.

The first deconvolution algorithms are termed inverse filters that determine the unknown object linearly by multiplications and divisions in Fourier space.

¹The choice of the coordinate system for the rotation parameters (α, β, γ) should be done carefully in order to avoid singularity in the parameterisation (Triggs et al. 2000). According to the previous work of (Brandt & Mevorah 2006) concerning micro-rotation imaging, we define the rotation parameters (α, β, γ) over the z -, x - and z -axes, respectively where α is the rotation angle on the image plane (ideally zero), β is the angle between the rotation axis and the projection direction (ideally $\pi/2$) and γ is the rotation angle around the rotation axis.

The simplest inverse filter functions by taking the Fourier transform of 3D images and dividing it by the Fourier transform of the PSF, mathematically represented by $F = G/H$ where F , H and G are the 3D spectral density of object f , image stack g and PSF h respectively. The utility of this method is limited by noise amplification as, during division in Fourier space, small values of high-frequency noise are amplified by the division operation. Another approach to compromise the noise amplification is Wiener filtering (Erhardt et al. 1958, Jain 1989), where the unknown object is computed by multiplying the spectrum of images with a set of optical transfer functions, i.e $F = H^*G/(H^*H + S)$ where $*$ is complex conjugate and S is the power spectrum of noise over object density. The limitation of the Wiener filter is that it does not generally provide optimal image quality due to the band-limited PSF and the presence of high-frequency noise. More importantly, the Wiener deconvolution, as it is understood in the classical sense, is not applicable in the micro-rotation imaging since due to the rotating geometry the imaging process, though being linear, is not shift invariant unlike the conventional through-stack imaging. As the consequence, the 3D Wiener deconvolution cannot be performed in the 3D Fourier domain by a simple product with a transfer function of the Wiener filter.

An alternative family of deconvolution algorithms is the nonlinear iterative algorithms which are introduced to improve the performance of inverse filters by incorporation of prior information about the unknown object. Most of the nonlinear deconvolution methods applied in fluorescence imaging solve the well-known Tikhonov functional $\hat{\mathbf{f}} = (\mathbf{H}^T\mathbf{H} + \lambda\mathbf{I})^{-1}\mathbf{H}^T\mathbf{g}$, iteratively where λ is the regularisation parameter and \mathbf{I} is the identity matrix. Many iterative algorithms, such as the Carrington's algorithm and the iterative constrained Tikhonov–Miller (ICTM) algorithms (Carrington 1990, van der Voort & Strasters 1995, Verveer & Jovin 1997b), solve the Tikhonov functional using conjugate gradient (CG) methods. These algorithms are named differently according to how their non-negativity constraint is implemented. Another family of iterative algorithms is developed using the statistical inversion theory to model measurement uncertainty and utilise prior knowledge. The methods are based on the concept of the maximum a posterior (MAP) and the expectation maximization (EM) estimates (see, for instance, Holmes 1989, Verveer et al. 1999, Vicidomini et al. 2006). In general, the statistical approaches are effective when the noise in images is fairly strong, but they yield at the cost of increased computational complexity.

Chapter 3

Reconstruction Methods

The problem of determining a 3D structure from multiple images consists of two subproblems: motion estimation to determine the motion parameters θ , and object density recovery to reconstruct the object structure \mathbf{f} . Although this thesis focuses on the latter problem, estimating the motion parameters, or equivalently image alignment, is crucial because inaccurate motion estimates will cause artefacts in resulting reconstruction, no matter what reconstruction methods we select.

The image alignment methods used in the thesis are based on the work of Palander (2007) who suggested three different approaches for estimating the motion parameters. The estimation methods include cross-correlation, feature-based and model-based methods. First, the cross-correlation method serves as an efficient tool for solving initial estimate of in-plane translation parameters ($\mathbf{t}_x, \mathbf{t}_y$) with fast and automatic computation. This method estimates motion parameters based on the assumption that two consecutive micro-rotation images are highly correlated, and therefore cross-correlation values between these images can be used for translation estimate. Second, the feature-based method is used to solve more general motion parameters, such as the in-plane translation¹ and the three angle parameters, at a higher cost of computation and some hyper-parameters need to be adjusted. The feature-base approach determines the motion parameters based on tracking correspondence information (object features such as edges, corners or blobs) extracted from adjacent images; This approach thus requires sufficient number of reliable features to obtain an accurate estimate. Finally, the model-based method is the most general, but also required heaviest computation, method which can fully solve the six motion parameters describing the 3D rotation. The method estimates the motion parameters simultaneously with the object structure by taking into account the PSF projection model (Brandt & Mevorah 2006, Brandt & Kolehmainen 2007, Yu et al. 2008). Because of the computational complexity, the model-based method is often used at the final state

¹Unfortunately, the depth translation parameters (\mathbf{t}_z) can not be recovered by the feature-based approach due to its implicit assumption for the straight-line projection.

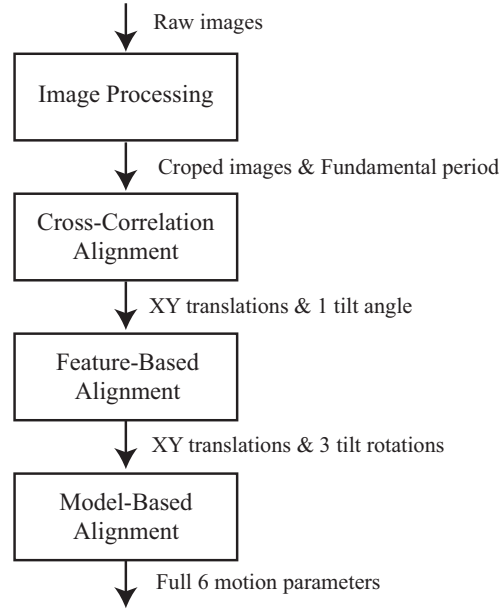


Figure 3.1: Hierarchical motion-estimation algorithm combining the cross-correlation, feature-based and model-based alignment methods. Image processing crops the region of interest in micro-rotation images, and determines the fundamental period (number of images for a full 360° rotation) using the 1D autocorrelation function for each image pixel through out the image sequence.

after good initial parameters are estimated by the correlation and feature-based methods. In conclusion, the motion estimate is achieved by using a single, hierarchical three-step algorithm that combines the three described methods together (Figure 3.1). In principle, to obtain a good reliability and accuracy in motion estimation, the micro-rotation image data should contain clear details.

Once the motion estimation has been solved, determining the object density \mathbf{f} in (2.6) is equivalent to solve a linear inverse problem. The following section will introduce the statistical theory used as a basis for developing the statistical reconstruction methods applied for micro-rotation imaging.

3.1 Statistical Methods

The image formation model (2.6) describes how the projection images \mathbf{m} can be constructed from the object density \mathbf{f} . However, this image formation model is not realistic because the image data and the model itself always contain various kinds of uncertainty. The uncertainty generally arises from many reasons, for example: measurement noise caused by the image acquisition process, model uncertainty occurred by inexact modelling of image formation, or from the inaccuracy of the alignment methods. A standard approach to characterise such uncertainties is to

use the statistical concept built on the Bayesian principle (Jaynes 2003) where all parameters of interest are treated as random variables. An alternative advantage of the Bayesian approach is that all the available prior knowledge relating to the unknown object can be used in a systematic way to solve the reconstruction problem. The statistical framework used in solving the reconstruction problem will be addressed in the following.

Statistical Framework

In statistical inverse problems, the complete solution \mathbf{f} in (2.6) can be represented by the posterior distribution $p(\mathbf{f}|\mathbf{m}, \boldsymbol{\theta})$, given by the Bayes' formula

$$p(\mathbf{f}|\mathbf{m}, \boldsymbol{\theta}) = \frac{p(\mathbf{m}|\mathbf{f}, \boldsymbol{\theta})p(\mathbf{f})}{p(\mathbf{m})} \propto p(\mathbf{m}|\mathbf{f}, \boldsymbol{\theta})p(\mathbf{f}) \quad (3.1)$$

where $p(\mathbf{m}|\mathbf{f}, \boldsymbol{\theta})$ is the likelihood density, $p(\mathbf{f})$ is the prior density for \mathbf{f} and the denominator $p(\mathbf{m})$ is a normalisation term, independent of \mathbf{f} , which often can be dropped. The likelihood function $p(\mathbf{m}|\mathbf{f}, \boldsymbol{\theta})$ contains the relationship between the measurement images and the object that characterises information about measurement noise and modelling uncertainties. The prior density $p(\mathbf{f})$ expresses our belief about the actual object density, prior to measurement of images \mathbf{m} . The construction of the likelihood and the prior density functions is described as follows.

Two commonly used assumptions for characterising measurement noise in fluorescence imaging are the Poisson and the Gaussian noise models. The Poisson model is based on the assumption that all recorded image values in \mathbf{m} are from an independent Poisson process with the mean value $(\mathbf{A}\boldsymbol{\theta}\mathbf{f})_j$. The corresponding likelihood function, which is the joint probability density function for the measurement data \mathbf{m} , is given by

$$p(\mathbf{m}|\mathbf{f}, \boldsymbol{\theta}) = \prod_{j=1} \left(\frac{1}{m_j!} \right) \exp \left(\mathbf{m}^T \log(\mathbf{A}\boldsymbol{\theta}\mathbf{f}) - \mathbf{1}^T \mathbf{A}\boldsymbol{\theta}\mathbf{f} \right), \quad (3.2)$$

where $\mathbf{1} = [1, 1, \dots, 1]^T$ is a vector whose elements equal to one. On the other hand, the Gaussian noise model is based on the assumption that all recorded image values in \mathbf{m} are from an additive, independent and identical Gaussian process, mathematically represented by $\mathbf{m} = \mathbf{A}\boldsymbol{\theta}\mathbf{f} + \mathbf{n}$ where the additive noise $\mathbf{n} \sim \mathcal{N}(\mathbf{n}|\mathbf{A}\boldsymbol{\theta}\mathbf{f}, \sigma_n^2)$ with the noise covariance σ_n^2 . The corresponding Gaussian likelihood density is thus written by

$$p(\mathbf{m}|\mathbf{f}, \boldsymbol{\theta}) \propto \exp \left(-\frac{\|\mathbf{m} - \mathbf{A}\boldsymbol{\theta}\mathbf{f}\|^2}{2\sigma_n^2} \right). \quad (3.3)$$

It should be noted that, for the high number of measured photon count, the

Object prior	$-\log p(\mathbf{f})$
Gaussian	$\lambda \ \mathbf{f}\ ^2$
Entropy	$\lambda(\mathbf{f}^T \log(\mathbf{f}/\mathbf{f}_0) - \mathbf{1}^T \mathbf{f})$
Total Variation (TV)	$\lambda \mathbf{1}^T \mathbf{G}\mathbf{f} $

Table 3.1: Prior functions used in reconstruction algorithms where λ is the prior strength or the regularisation parameter, \mathbf{f}_0 is the initial object which, in practice, is often selected as a constant value. The operations between two vectors are performed element by element.

Poisson noise model can be approximated by the Gaussian model (Calvetti & Somersalo 2007).

In the case of the prior density $p(\mathbf{f})$, we consider three statistical functions: the Gaussian, the entropy and the spatial-derivative priors (Table 3.1). The Gaussian prior is a widely used prior in fluorescence imaging, through its well-known properties for preventing noise amplification and providing smooth structure in the solution. The Gaussian density can be also seen as the Tikhonov functional in the traditional regularisation problem. The entropy function is another common prior that has been widely applied for image restoration in astronomy (Skilling & Bryan 1984, Gull & Skilling 1999) and to some extent in electron microscopy (Frank 2006). According to Skilling (1989), the entropy distribution is optimal for non-negative functions in the absence of further prior knowledge.

Another choice for the prior density is spatial-derivative priors which are in general derived from the Markov random fields theory (Kaipio & Somersalo 2004). The derivative priors have been highly successful in fluorescence imaging due to its ability to suppress high-frequency noise in measurement images, while the edges of object of interest remain sharp (the edge-preservation property) (Dey et al. 2006, Vicidomini et al. 2006). In this thesis, we thus use the spatial-derivation prior with the total variation (TV) function defined by

$$\begin{aligned}
 V(\mathbf{f}) &= \int |\Delta f(\mathbf{r})| d\mathbf{r} \approx \sum_l \left| \sum_k \xi_l \Delta g(\mathbf{r}_l - \mathbf{r}_k) \right|, \\
 &\approx \mathbf{1}^T |\mathbf{G}\mathbf{f}|,
 \end{aligned} \tag{3.4}$$

where Δ is the Laplacian operator, $f(\mathbf{r}) = \sum_k \xi_k g(\mathbf{r} - \mathbf{r}_k)$ is the piecewise continuous object density with the Gaussian kernel $g(\mathbf{r})$ and $\mathbf{f} = [\xi_1, \xi_2, \dots, \xi_N]^T$, \mathbf{G} is the Toeplitz matrix representing the 3D convolution with the Laplacian of Gaussian kernel Δg . Now, the TV regularised prior takes the form

$$p(\mathbf{f}) \propto \exp(-\lambda V(\mathbf{f})) = \exp(-\lambda \mathbf{1}^T |\mathbf{G}\mathbf{f}|), \tag{3.5}$$

which λ is the regularisation parameter choosing according to the noise level in the measurement. Since the function taking the absolute value is not differentiable at zero, we use the smooth approximation $|t| \approx \beta^{-1} \log(\cosh(\beta t))$ in the object prior (3.5), as introduced by Green (1990) and Kolehmainen et al. (2003). In Publication 3, we have demonstrated that this TV prior (3.5) can produce competitive reconstruction quality with the spatial-derivative prior, proposed by Green (1990) in positron emission tomography.

Structure Estimation

Once the posterior distribution has been constructed through the likelihood and the prior functions, an efficient parameter estimation is required for characterising the posterior distribution. Two widely used estimates in the Bayesian framework are the conditional mean (CM) and the maximum a posteriori (MAP) methods (Kaipio & Somersalo 2004). In high dimensional problems such as 3D image reconstruction, the use of CM estimate is problematic because of the required heavy computation of the CM integral, which in practice need to be numerically evaluated by using sampling techniques such as the Markov chain Monte Carlo (MCMC) method. An example where image reconstruction problem is solved using sampling techniques can be found, for instance, in single photon emission tomography (Green 1990, Weir 1997). Due to the computational complexity, parameter estimation for 3D image reconstruction is often done using the MAP estimate.

In this study, we thus compute the MAP estimate

$$\hat{\mathbf{f}} = \arg \max_{\mathbf{f}} p(\mathbf{f})p(\mathbf{m}|\mathbf{f}, \boldsymbol{\theta}), \quad (3.6)$$

which means that, for the given prior density $p(\mathbf{f})$ and the measurement data \mathbf{m} , we determine the unknown values \mathbf{f} which approximate the data \mathbf{m} the best. In this way, the computation of the MAP estimate (3.6) is equivalent to minimise the cost function

$$q(\mathbf{f}) = c(\mathbf{f}) + s(\mathbf{f}) \quad (3.7)$$

where $c(\mathbf{f}) = -\log p(\mathbf{m}|\mathbf{f})$ is the likelihood term and $s(\mathbf{f}) = -\log p(\mathbf{f})$ is the prior term. Hence, the MAP estimate can be seen as the traditional estimates with additional regularisation (Calvetti & Somersalo 2007). Furthermore, since the likelihood functions and the prior functions described above are concave, the posterior functions will be also concave and therefore a global maximum can be found.

Now, there are several ways to compute the MAP estimate (3.6). One possibility is direct numerical optimisation using either the first order (line search) methods or the second order (trust region) methods (Nocedal & Wright 2006). An alternative approach is to use a closed-form iterative solution which is, for instance,

derived from the expectation-maximization method (Dempster et al. 1977). These two approaches are the main topics in Publication 2 and Publication 3, and will be discussed in the following two sections.

3.1.1 Optimisation: Generalised Skilling-Bryan Method

Numerical optimisation is a task for finding minimum (or maximum) location(s) of a cost function. Optimisation methods can be categorised in two classes: line search and trust region methods. The line search methods search for a solution in a single direction in each iteration, whereas the trust-region methods compute the iterates in a high-dimensional space. In other words, line search methods fix the direction and then evaluate an appropriate moving distance, but trust region methods first choose a maximum moving distance and thereafter searches for a local minimum location, subject to the distance constraint. In general, trust region methods converge faster and tend to be more robust than line search methods (Nocedal & Wright 2006).

In deconvolution fluorescence microscopy, line search methods such as the conjugate gradient method have been widely applied for computing the MAP estimate (Carrington et al. 1995, van der Voort & Strasters 1995, Verveer & Jovin 1997a, van Kempen et al. 1997, Markham & Conchello 2001). The conjugate gradient method becomes popular due to its ability to iteratively solve a large system of linear equations whose matrix is symmetric and positive definite. Since the physical quantities of the unknown object \mathbf{f} are non-negative, most of these algorithms have been implemented the non-negativity constraint by simply projecting negative values to zero after each iteration. Except that Carrington et al. (1995) used the Kuhn–Tucker condition and Verveer et al. (1999) used the parameter transformation $\mathbf{f} = \mathbf{x}^2$ to ensure the non-negativity constraint.

In contrast to the line search techniques above, Skilling & Bryan (1984) developed a complicated but highly successful scheme, which repetitively searches for a minimum of the cost function in a small dimensional subspace, instead of a single search direction or a high-dimensional full space. This method has been widely used in solving image deconvolution problems in astronomy and medical imaging (Skilling 1989, Jannetta et al. 2004), because of the ability to solve non-linear cost functions with the non-negativity constraint. However, the *original* Skilling–Bryan method restricts to minimise the statistical cost function which assumes the Gaussian noise model and the entropy prior functional. It would be useful to generalise this method to be used with the Poisson noise model and the other prior functions, for instance, the ones described in Table 3.1. The generalisation of the Skilling–Bryan method is the topic of the Publication 2 and its principle is summarised as follows.

Algorithm

The cost function (3.7) can be approximated with the second-order Taylor expansion. Then the vector \mathbf{p} is selected so that the posterior cost function q is minimised, i.e.,

$$\min_{\mathbf{p}} q(\mathbf{f} + \mathbf{p}) = q(\mathbf{f}) + \mathbf{g}_q^T \mathbf{p} + \frac{1}{2} \mathbf{p}^T \mathbf{H}_q \mathbf{p}, \quad (3.8)$$

where \mathbf{g}_q and \mathbf{H}_q are the gradient vector and the Hessian matrix of the cost function q . Searching for the vector \mathbf{p} in a high dimensional space is costly. To obtain an efficient computation, Skilling and Bryan suggested minimising the cost function in the trust subspace defined by three basis vectors ($\mathbf{e}_1, \mathbf{e}_2, \mathbf{e}_3$). The selection of these basis vectors is the key idea of the Skilling–Bryan optimisation that will be discussed in the following.

The solution \mathbf{p} for (3.8) is

$$\mathbf{p} = (\mathbf{H}_q + \gamma \mathbf{I})^{-1} \mathbf{g}_q, \quad (3.9)$$

$$\approx (\mathbf{I} + \gamma^{-1} \mathbf{H}_q) \mathbf{g}_q = \mathbf{g}_s + \mathbf{g}_c + \gamma^{-1} (\mathbf{H}_s + \mathbf{H}_c) (\mathbf{g}_s + \mathbf{g}_c), \quad (3.10)$$

where the matrix inversion is approximated up to the second-order, γ is a constant, and $\mathbf{g}_c, \mathbf{g}_s, \mathbf{H}_c$ and \mathbf{H}_s are the gradient vectors and the Hessian matrices of the likelihood function c and the prior function s . Obviously, the search vector \mathbf{p} is just a linear combination of the six vectors ($\mathbf{g}_c, \mathbf{g}_s, \mathbf{H}_c \mathbf{g}_c, \mathbf{H}_s \mathbf{g}_s, \mathbf{H}_s \mathbf{g}_c$ and $\mathbf{H}_c \mathbf{g}_s$) in the approximation. In practice, the linear combination of the last four terms can be used as one search direction. Thus, we obtain the three search directions

$$\mathbf{e}_1 = \mathbf{f} \mathbf{g}_s, \quad \mathbf{e}_2 = \mathbf{f} \mathbf{g}_c, \quad \mathbf{e}_3 = \mathbf{f} \mathbf{H}_c \left(\frac{\mathbf{e}_1}{\|\mathbf{g}_s\|} + \frac{\mathbf{e}_2}{\|\mathbf{g}_c\|} \right) + \mathbf{f} \mathbf{H}_s \left(\frac{\mathbf{e}_1}{\|\mathbf{g}_s\|} + \frac{\mathbf{e}_2}{\|\mathbf{g}_c\|} \right),$$

which define a 3D subspace. The vector multiplications and divisions are performed element by element.

The gradient directions \mathbf{g}_s and \mathbf{g}_c are replaced by $\mathbf{f} \mathbf{g}_s$ and $\mathbf{f} \mathbf{g}_c$ to increase the weight for high values in order to achieve the positivity constraint. In the third direction, the normalisation by the length of gradient vector is performed before multiplying with the Hessian matrix. Note that, solving the search vector \mathbf{p} from (3.9) corresponds to the Levenberg-Marquardt method, whereas using the first-order Taylor approximation is equivalent to optimisation using line search methods (Nocedal & Wright 2006).

Within the 3D subspace, the search vector \mathbf{p} is

$$\mathbf{p} = \mathbf{E} \mathbf{x} = x_1 \mathbf{e}_1 + x_2 \mathbf{e}_2 + x_3 \mathbf{e}_3, \quad (3.11)$$

where the matrix $\mathbf{E} = [\mathbf{e}_1 \ \mathbf{e}_2 \ \mathbf{e}_3]$ and the coefficient vector $\mathbf{x} = [x_1, x_2, x_3]^T$. Now, we determine \mathbf{x} in this subspace that gives the minimum of s subject to the

constraint² c_{aim} . In order to estimate the minimum s in the 3D subspace, the three-element gradients and nine-element Hessian need to be computed, and the minimum in the subspace is estimated by simply solving three linear equations with a procedure for controlling the non-negativity constraint. For details, see (Skilling & Bryan 1984). Finally, the current \mathbf{f} is moved to the new location by $\mathbf{f}_{\text{new}} = \mathbf{f} + \mathbf{E}\mathbf{x}$. The iteration is repeated until the aim $c = c_{\text{aim}}$ is achieved or the maximum number of iterations is reached.

In summary, the main features of the Skilling–Bryan method is that (1) a subspace of several search directions is used instead of a line search or a high-dimensional space and (2) the method inherently enforces the positivity constraint during each subspace search. These features make the extended algorithm attractive for solving high-dimensional, nonlinear problems with the positivity constraint. Compared to line search methods, the optimisation scheme requires much less number of iterations but each iteration consists of six projection and backprojection ($\mathbf{A}_{\boldsymbol{\theta}}^T \mathbf{A}_{\boldsymbol{\theta}}$) pairs. So constructing the more sophisticated search directions is made on the expense of more frequent evaluation of the image formation model. As a drawback, the Skilling–Bryan algorithm requires to compute the Hessians of the cost functions that can be problematic when the Hessians are not analytically available. In principle, the generalised Skilling–Bryan algorithm is also appropriate for solving the wide class of measurement noise and prior models within the Bayesian framework.

3.1.2 Expectation Maximisation Method

The expectation maximisation (EM) algorithm for image reconstruction has become popular in the fields of astronomy and biomedical imaging (McLachlan & Krishnan 2008). Initially, it was derived from Bayesian principle in the early 1970’s by Richardson (1972) and Lucy (1974). In the early 1980’s it was re-derived by Shepp & Vardi (1982) as an iterative algorithm for solving problems in positron emission tomography (PET), assuming a photon emission process with Poisson statistics. The iterative scheme is a maximum likelihood solution that was derived from the expectation maximisation algorithm of Dempster et al. (1977). Thereafter, Holmes (1989) applied the photon emission principle into fluorescence microscopy and later the EM algorithm becomes a widely used algorithm for image restoration in this field. The reason for its popularity is that the EM algorithm provides an elegant closed-form iterative solution and the apparent ability to produce reconstructed images with good quality in the presence of high noise levels (Conchello 1998). The EM algorithm is the topic of the Publication 3 and its mathematical concept is briefly discussed in the following.

²The constant c_{aim} is proportional to the noise level in the images. For the Gaussian noise model, c_{aim} is equal to $N\sigma^2$ where σ^2 is the noise variance and N is the number of measurement data. The Poisson case is more difficult, one possibility is to select the Csiszár I-divergence (Csiszár 1991) as c_{aim} .

Algorithm

The principle of the EM algorithm is based on the maximum likelihood (ML) estimate of unknown parameters, given observations with missing information, or incomplete data. The EM algorithm introduces a set of complete but unobservable data \mathbf{z} that relates the incomplete observed data \mathbf{m} to the object \mathbf{f} . The algorithm first estimates the conditional mean of the complete-data log likelihood $\log p(\mathbf{z}|\mathbf{f})$ from incomplete data \mathbf{m} and the current estimate \mathbf{f}_k (expectation step) and second, maximises the expected complete-data likelihood with respect to the object (maximisation step):

$$\begin{aligned} \text{E-step: } & Q(\mathbf{f}|\mathbf{f}_k) = E_{\mathbf{z}|\mathbf{m}}[\log p(\mathbf{z}|\mathbf{f})|\mathbf{m}, \mathbf{f}_k], \\ \text{M-step: } & \mathbf{f}_{k+1} = \arg \max_{\mathbf{f}} Q(\mathbf{f}|\mathbf{f}_k), \end{aligned} \quad (3.12)$$

where k denotes the iteration index.

In the photon-emission reconstruction problem the complete data is defined as $\mathbf{z} = \{\{z_{ij}\}_{j=1}^N\}_{i=1}^M$ where each z_{ij} denotes the emissions from voxel j detected by detector element i . Assuming that the complete data z_{ij} are independent Poisson distributed random variables, the E-step in (3.12) can be written as $Q(\mathbf{f}|\mathbf{f}_k) = \mathbf{f}_k \left(\mathbf{A}_{\theta}^T \frac{\mathbf{m}}{\mathbf{A}_{\theta} \mathbf{f}_k} \right) \log \mathbf{f}(\mathbf{A}_{\theta}^T \mathbf{1}) - \mathbf{f}(\mathbf{A}_{\theta}^T \mathbf{1})$ and the M-step becomes the well-known, EM iterative algorithm

$$\mathbf{f}_{k+1} = \frac{\mathbf{f}_k}{\mathbf{A}_{\theta}^T \mathbf{1}} \left(\mathbf{A}_{\theta}^T \frac{\mathbf{m}}{\mathbf{A}_{\theta} \mathbf{f}_k} \right), \quad (3.13)$$

where $\mathbf{1} = [1, 1, \dots, 1]^T$, k is the iteration index and the vector divisions and multiplications are performed element by element. The iteration goes as follows: (1) create initial volume \mathbf{f}_0 , often equal a positive constant, (2) divide data images \mathbf{m} elementwise by the projected images $\mathbf{A}_{\theta} \mathbf{f}_0$, (3) multiply the backprojected volume $\mathbf{A}_{\theta}^T \frac{\mathbf{m}}{\mathbf{A}_{\theta} \mathbf{f}_0}$ elementwise by the initial \mathbf{f}_0 , and (4) finally dividing the resulting 3D volume elementwise by $\mathbf{A}_{\theta}^T \mathbf{1}$ to update the next estimate \mathbf{f}_{k+1} . The four steps are repeated until convergence or reaching the chosen maximum number of iteration.

An attractive feature of the EM algorithm is that the updates force a natural non-negativity constraint. This feature is not shared by the gradient-based method or the trust region methods where the implementation of a non-negativity condition on these methods requires a careful handling (Skilling & Bryan 1984, Verveer & Jovin 1997b). Another characteristic of the EM algorithm is that the likelihood increases monotonically during the EM iterations, although its convergence is relatively slow Dempster et al. (1977).

The EM algorithm can be directly extended to incorporate with prior functions using the generalised EM method, coinciding with the MAP estimate (Dempster et al. 1977). The treatment of the complete data remains unchanged, so that the

E-step given in (3.12) is the same. However, the M-step maximises the log posterior given the complete data \mathbf{z} , i.e. $\mathbf{f}_{k+1} = \arg \max_{\mathbf{f}} \{Q(\mathbf{f}|\mathbf{f}_k) - \log p(\mathbf{f})\}$. Green (1990) proposed a one-step-late algorithm to the MAP estimate in the PET problem that yields the iterative scheme

$$\mathbf{f}_{k+1} = \frac{\mathbf{f}_k}{\mathbf{A}_{\theta}^T \mathbf{1} + \lambda \nabla V(\mathbf{f}_k)} \left(\mathbf{A}_{\theta}^T \frac{\mathbf{m}}{\mathbf{A}_{\theta} \mathbf{f}_k} \right), \quad (3.14)$$

where λ is the regularisation parameter and V is a spatial-derivative function. Thereafter, Dey et al. (2006) and Vicidomini et al. (2006) introduced this algorithm in the field of fluorescence microscopy (through-stack imaging), with alternative derivative-prior functions V . By contrast, Publication 3 applied the iterative scheme (3.14) with the TV prior (3.5) for solving image reconstruction in micro-rotation fluorescence microscopy and, in this thesis, we call it the EMTV algorithm.

Parameter Selection

A difficulty in the use of the MAP approach, such as (3.14), is the selection of the regularisation parameters, or equivalently, the hyperparameter of the prior. If λ is too large, the prior tends to over-smoothing in the solution, whereas too small λ leads noise amplification and instability in the solution. There are several methods available for selecting λ in through-stacking image restoration, for instance, constrained least square, generalised cross validation (GCV) and maximum likelihood (Galatsanos & Katsaggelos 1992). The numerical comparison between these methods has been demonstrated by van Kempen & van Vliet (1999) who concluded that the CGV seems to be the most accurate for estimating the regularisation parameter. These method is however restricted to the Gaussian noise assumption with the Gaussian prior. The analytical solution for the Poisson noise assumption is not available. van Kempen & van Vliet (1999) suggested to linearise the Poisson likelihood using a Taylor series expansion that yields an approximated solution, which linearly depends on the Gaussian solution obtained by the GCV method. The similar approximation for determining the regularisation parameter for the Gaussian likelihood with the entropy prior can be found in Thompson (1988).

All the described methods for estimating λ in through-stack imaging require to solve the restored 3D image, which is usually estimated by the non-iterative Wiener filter. Unfortunately, the Wiener solution is not analytically available for micro-rotation imaging. One possibility is to use the iterative reconstruction methods, such as EM algorithms, for estimating the micro-rotation reconstruction. The iterative methods is however computationally expensive compared to the Wiener filter due to the required repeatedly computation of the image formation model. Therefore, in practice the selection of λ is often done in an heuristic way through visual inspection of the resulting reconstruction.

Various forms of the EM algorithm

The original EM algorithm has been extended into many forms for different purposes. For instance, Conchello & McNally (1996) proposed to incorporate the EM algorithm with the Gaussian prior. This algorithm is similar to the original EM algorithm unless a modification is introduced before the update: $\mathbf{f}_{k+1} = (-1 + \sqrt{1 + 2\lambda\mathbf{f}_{k+1}})/\lambda$ where \mathbf{f}_{k+1} is given in (3.13). By using the L'Hopital's rule, we notice that the update \mathbf{f}_{k+1} remain unchanged when λ goes to zero. As the nature of Gaussian prior, this algorithm suppresses high-frequency noise in images as well as smooths out all structures including object's edges.

An alternative form to the original EM algorithm is the OSEM (ordered-subsets EM) algorithm, which provides remarkable improvement in convergence rates in the early iterations Hudson & Larkin (1994). The principle of the OSEM algorithm is that, for each OSEM iteration, the update uses only a subset of the data in which each subset typically consists of a group of images. The selection of subset is crucial as it effects convergence rates of the algorithm (Byrne 1998, Sotthivirat & Fessler 2003). Subset balance is recommended by Hudson & Larkin (1994), that is, each group of images should contain uniformly distributed projection directions around the object. Although the convergence of the OSEM algorithm is not guaranteed, it is the most widely used iterative method in emission tomography that demonstrates the success of the OSEM. A further research direction therefore is to investigate the applicability of the OSEM algorithm to the micro-rotation application.

The EM algorithm has been also developed for *blind deconvolution*, which is the term given to a image restoration method that estimates the object simultaneously with the PSF (Holmes 1992, Holmes et al. 2006). This algorithm contains two deconvolution steps: first initial PSF and estimate the object using the ordinary EM algorithm (3.13) for a specific number of EM iteration and, second using the estimated object to compute the PSF using the EM iteration in the reciprocal way. The second step is essentially an inverse of the original EM algorithm, as the object and PSF have reverse roles. As the two EM iterations are required for a complete loop, the additional computation for EM blind deconvolution becomes unavoidable. A comparison between the EM and the Wiener-filter blind deconvolution can be found in Fish et al. (1995) and the results demonstrated the robustness and high-noise tolerance of the EM blind algorithm. As a future work, it would be interesting to investigate whether the EM blind deconvolution could be applied for micro-rotation imaging and give any significant improvement in the reconstruction quality.

3.1.3 Reconstruction with Motion Uncertainty Model

The reconstruction methods described in the previous subsections require prior knowledge of the motion parameters θ that describe the positions and orienta-

tions of 3D object. The motion parameters can be estimated using, for instance, the correlation alignment and the feature-based methods (Frank & McEwen 1992, Brandt & Mevorah 2006, Palander 2007). However, no matter what methods we select, there is always some inaccuracy, or uncertainty, in the estimated parameters that causes artefacts in the reconstruction. Our hypothesis is thus that the quality of the reconstruction would be better if we take not only the motion estimates but also their uncertainty into consideration in the reconstruction phase. Incorporating motion uncertainty into the reconstruction process is the main topic of Publication 4 where its principle is summarised in the following.

Algorithm

In the Bayesian framework, it is straightforward to create the joint posterior distribution $p(\mathbf{f}, \boldsymbol{\theta}|\mathbf{m})$ of the object density and the motion parameters, given the measurement images. However, in the reconstruction problem, only the object density is of our interest where the motion parameters can be seen as nuisance parameters. To eliminate the nuisance parameters we compute the marginal posterior distribution $p(\mathbf{f}|\mathbf{m})$ by integrating the joint distribution $p(\mathbf{f}, \boldsymbol{\theta}|\mathbf{m})$ over $\boldsymbol{\theta}$, i.e.,

$$p(\mathbf{f}|\mathbf{m}) = \int p(\mathbf{f}, \boldsymbol{\theta}|\mathbf{m}) d\boldsymbol{\theta} \propto \int p(\mathbf{f}, \boldsymbol{\theta})p(\mathbf{m}|\mathbf{f}, \boldsymbol{\theta}) d\boldsymbol{\theta}, \quad (3.15)$$

where $p(\mathbf{m}|\mathbf{f}, \boldsymbol{\theta})$ is the likelihood function and $p(\mathbf{f}, \boldsymbol{\theta})$ is the joint prior distribution of the object density and the motion parameters.

Assuming independence between the prior distribution of the object density $p(\mathbf{f})$ and the prior distribution of the motion parameters $p(\boldsymbol{\theta})$, the marginal posterior in (3.15) can be written as

$$p(\mathbf{f}|\mathbf{m}) \propto p(\mathbf{f})p(\mathbf{m}|\mathbf{f}), \quad (3.16)$$

where $p(\mathbf{m}|\mathbf{f})$ is the marginal likelihood

$$p(\mathbf{m}|\mathbf{f}) = \int p(\boldsymbol{\theta})p(\mathbf{m}|\mathbf{f}, \boldsymbol{\theta}) d\boldsymbol{\theta}. \quad (3.17)$$

The models (3.16) and (3.17) provide us the basis of incorporating the motion uncertainty model $p(\boldsymbol{\theta})$ into the reconstruction problem, as the recovery of camera parameters are often assumed independent from the reconstruction problem. In the following, we show how to construct of the marginal likelihood $p(\mathbf{m}|\mathbf{f})$ and thereafter the object structure prior $p(\mathbf{f})$.

To construct the marginal posterior $p(\mathbf{m}|\mathbf{f})$, we need the likelihood function $p(\mathbf{m}|\mathbf{f}, \boldsymbol{\theta})$, and the motion uncertainty distribution $p(\boldsymbol{\theta})$ appearing in the integral (3.17). For the likelihood function $p(\mathbf{m}|\mathbf{f}, \boldsymbol{\theta})$, we assume *i.i.d.* Gaussian noise with the isotropic covariance in the measurement images, mathematically written as $p(\mathbf{m}|\mathbf{f}, \boldsymbol{\theta}) \sim \mathcal{N}(\mathbf{m}|\mathbf{A}_{\boldsymbol{\theta}}\mathbf{f}, \mathbf{I})$ where the normalised noise covariance matrix can be

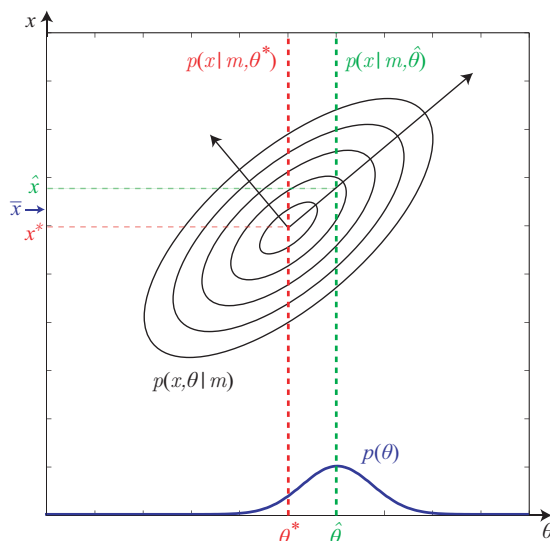


Figure 3.2: A sketch showing how marginalisation improves solution in a simple 2D problem. Here $p(x, \theta|m)$ is a joint posterior density of the parameters x and θ for a given data m , where the maximum of the joint density is achieved at (x^*, θ^*) and $p(\theta)$ is an uncertainty distribution (prior) centred at $\hat{\theta}$. The maximum a posteriori (MAP) solution for x given $\hat{\theta}$ yields the estimate \hat{x} . Obviously, uncertainty in estimating θ leads to the difference $x^* - \hat{x}$ between the maxima. If we take the uncertainty distribution $p(\theta)$ into account, we can determine x that maximises the integral of $p(x, \theta|m)$ over θ , that is $\bar{x} = \arg \max \int p(x|m, \theta)p(\theta) d\theta$. The marginal solution \bar{x} locates closer to the maximum x^* where the improvement depends on the shape and orientation of the joint posterior distribution $p(x, \theta|m)$.

obtained by performing normalisation over image intensities. The prior $p(\theta)$ is assumed to be *i.i.d.* Gaussian with the centre at $\hat{\theta}$ and the covariance matrix \mathbf{C} , that is $p(\theta) \sim \mathcal{N}(\theta|\hat{\theta}, \mathbf{C})$. The Gaussian model is reasonable, especially when the maximum likelihood estimator (MLE) is used for solving the motion parameters $\hat{\theta}$, since the MLE is asymptotically normal under relatively mild regularity conditions (Karr 1993).

Thus, the marginal posterior takes the form

$$p(\mathbf{f}|\mathbf{m}) \propto p(\mathbf{f}) \int \exp \left(-\frac{1}{2} \|\mathbf{m} - \mathbf{A}_\theta \mathbf{f}\|^2 - \frac{1}{2} (\theta - \hat{\theta})^T \mathbf{C}^{-1} (\theta - \hat{\theta}) \right) d\theta, \quad (3.18)$$

where $\hat{\theta} = [\hat{\theta}_1^T, \dots, \hat{\theta}_K^T]^T \in \mathbb{R}^{6K}$ is a joint vector of the pre-estimated motion parameters for the K projections, and the covariance matrix $\mathbf{C} \in \mathbb{R}^{6K \times 6K}$ characterises the degree of uncertainty in the estimated values $\hat{\theta}$. The covariance matrix \mathbf{C} can be obtained as by-product of the motion estimation methods. A simple example visualising the basic idea behind (3.18) is illustrated in Figure 3.2.

To make the integral (3.18) analytically tractable, the nonlinear projection

matrix \mathbf{A}_θ requires linearisation over the motion parameter using the Taylor series expansion. The resulting linear term in the exponential can be then integrated over θ using the Gaussian integral identity (for detail, see Publication 4). Inserting the resulting integral (3.18) and the TV prior (3.5) into the MAP estimate (3.6), we obtain the cost function q to be minimised over the object density \mathbf{f} :

$$q_{\text{unc}}(\mathbf{f}) = \lambda \mathbf{1}^T |\mathbf{G}\mathbf{f}| + \|\mathbf{m} - \mathbf{A}_{\hat{\theta}}\mathbf{f}\|^2 - \mathbf{g}^T \Sigma_{\mathbf{f}}^{-1} \mathbf{g}, \quad (3.19)$$

where $\Sigma_{\mathbf{f}} = \mathbf{B}_{\mathbf{f}}^T \mathbf{B}_{\mathbf{f}} + \mathbf{C}^{-1} \in \mathbb{R}^{6K \times 6K}$, $\mathbf{g} = \mathbf{B}_{\mathbf{f}}^T (\mathbf{m} - \mathbf{A}_{\hat{\theta}}\mathbf{f}) \in \mathbb{R}^{6K}$ and $\mathbf{B}_{\mathbf{f}}$ is the combination of derivative matrices of \mathbf{A}_θ with respect to the motion parameters θ . The formulation (3.19) can be seen as the standard MAP estimate supplied with an extra regularisation term, which depends on the confidence in the estimated motion parameters. The higher the confidence in the motion estimates, the closer to zero the extra term will be (the motion parameter distribution shrinks to a point).

There are several ways to minimise the objective function (3.19). One can use the second-order optimisation methods that require to construct the Hessian or approximated Hessian of the cost function. However, the construction of the (approximated) Hessian matrix could be complex and lead to excessive computation. To avoid too heavy complexity, we select a nonlinear (Pok-Ribiere) conjugate gradient (CG) algorithm instead with an explicit line search method (Pytlak 1998). The iteration is stopped when the change in L_2 -norm between two consecutive iterations is smaller than the threshold 10^{-4} , or the algorithm reaches the maximum number of iterations. The non-negativity constraint is implemented by projecting the negative values to zero after each iteration.

Marginalisation in Other Applications

In addition to the micro-rotation application, Bayesian marginalisation has been applied in image super-resolution problems where several low-resolution images are fused to obtain a single high-resolution image (Tipping & Bishop 2003, Pickup et al. 2007). Tipping & Bishop (2003) considers an image registration problem where the object intensities are integrated out from the posterior, yielding an improvement in the registration accuracy. On other hand, Pickup et al. (2007) overcomes registration uncertainty by integrating the posterior distribution over the registration and imaging parameters that results a slight improvement in the quality of the fused image. The latter approach is closely related to our proposed method, but it considers a 2D image-fusion problem and merely takes translation uncertainty into account.

In conclusion, the marginalisation method estimates the object structure by considering all the likely realisations for camera motion by utilising not only a single estimate for the motion but also its covariance estimate. This marginalisation procedure makes the reconstruction of the 3D structure more robust to errors

caused by inaccurate camera geometry. Due to the nonlinear approximation of the projection model, the performance of the proposed method relies on the degree of nonlinearity in the projection model and also how well the Gaussian model describes the motion parameter distribution. As it is natural, the marginalisation method gives only minor improvement when the motion parameters have been accurately recovered. Due to its general nature the marginalisation method is also directly applicable in other imaging applications that involve reconstruction of object densities from multiple projection images and suffer from high uncertainty in camera geometry.

3.2 Fourier Method

It has been shown in Section 3.1 that the statistical reconstruction methods have capability to incorporate prior knowledge about the object, to model measurement noise, as well as to handle uncertainty in the estimated motion parameters. The statistical methods, however, suffer from computational complexity, which is about about $O(N \log N)$ per iteration for the reconstruction N voxels and even more expensive for the reconstruction with the motion uncertainty model. The source of computational complexity arises due to the required *repetitive* computation of the statistical methods for calculating object-to-image and image-to-object transformations.

To overcome the computational complexity, Publication 5 suggests a two step solution for *confocal* imaging: first, individual confocal images are rapidly deconvoluted by 2D deconvolution using only a 2D PSF (Larson 2002, Biggs 2004) and second, we propose a non-iterative Fourier-based method to bring the reconstruction into the Cartesian coordinates from the cylindrical coordinates. The Fourier-based method has *dual* relationship to the classical filtered backprojection (FBP) method which is a standard reconstruction method in X-ray tomography (computed tomography or CT). The duality arises due to that projection images in CT are parallel projections of the object, whereas ideal confocal images represent the central slices of object corresponding to the focal plane, as shown in Figure 3.3(a,c). In X-ray tomography, the relationship between the projection images and the 3D object is described by the Fourier slice theorem which states that the Fourier transform of a CT image is equal to the central slice of the 3D object spectrum (Kak & Slaney 1988). By contrast, in the micro-rotation application, the confocal images and the 3D object are related by *dual* Fourier slice theorem. That is, the Fourier transform of a confocal image is equal to the parallel projection of the object spectrum as Figure 3.3c–d illustrates.

The principle of the FBP algorithm involves filtering of projection images and backprojecting the filtered images in the spatial domain (Kak & Slaney 1988, Jain 1989). In dual filtered backprojection (DFBP), rather than operating in the spatial domain, the method filters confocal image spectra and backprojects the

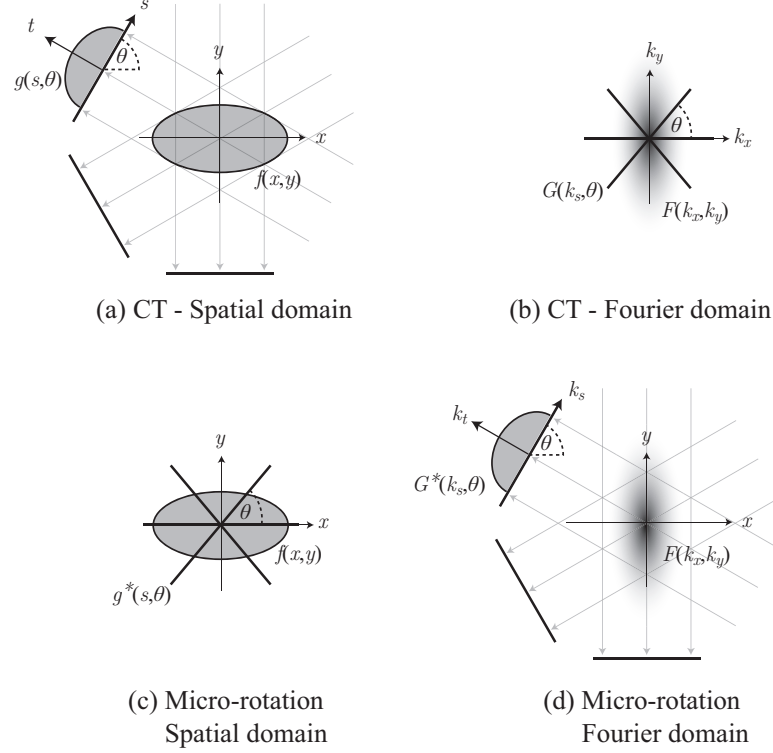


Figure 3.3: Comparison of the computed tomographic and the micro-rotation confocal projection models. The right column illustrate the Fourier transform of the projections, related by the Fourier slice theorem.

filtered spectra in the frequency domain instead (Figure 3.3d). The importance feature of the DFBP is that the operations, filtering and backprojecting, are performed in the same manner in the dual domain. As a consequence, the DFBP algorithm has computational complexity $O(N)$ which is equivalent to the linear complexity of the FBP. The complete mathematical derivation and practical implementation of the DFBP algorithm can be found in Publication 5 where the resulting formulation is summarised in the following.

Algorithm

The mathematical formulation of FBP can be represented by

$$f(x, y) = \int_0^\pi \int_{-\infty}^\infty |k_s| G(k_s, \theta) e^{j(x \cos \theta + y \sin \theta) k_s} dk_s d\theta \quad (3.20)$$

where $f(x, y)$ is the 2D object function, $G(k_s, \theta) = \mathcal{F}_s\{g(s, \theta)\}$ is the Fourier transform of 1D projection data $g(s, \theta)$ of the object f at angle θ , and \mathcal{F} is the Fourier transform with respect to the subscript (see Figure 3.3a–b). The multiplication with $|k_s|$ in the Fourier space represents a filtering operation whereas

the integration over θ is the backprojection step. Now, using the duality the dual formula of FBP is

$$F(k_x, k_y) = \frac{1}{(2\pi)^2} \int_0^\pi \int_{-\infty}^\infty |s| g^*(s, \theta) e^{-j(k_x \cos \theta + k_y \sin \theta)s} ds d\theta \quad (3.21)$$

where $F(k_x, k_y) = \mathcal{F}_y\{\mathcal{F}_x\{f(x, y)\}\}$ and $g^*(s, \theta) = f(s \cos \theta, s \sin \theta)$ is the 1D central slice of object f at angle θ (see Figure 3.3c–d). As can be seen, the DFBP operations are performed in the dual way: filtering the projection spectra and then backprojecting the filtered spectra in the frequency domain.

To achieve good-quality reconstruction, the DFBP algorithm requires a good stability of cell rotation, such that the rotation axis locates approximately on the focal plane. The cell rotation is a sensitive process since the non-adherent cells flow freely in suspension apart from the force included by the electric field of the cell rotator. However, careful image acquisition improves the rotation stability: an example of situation where the rotation stability is satisfactory is provided by Renaud et al. (2008) who demonstrated that the cell rotator is capable of reproducing high correlation images of the cell after a complete rotation 360° (with 90° stepwise). With sufficient rotation stability, the acquired images can be accurately aligned using, for instance, a 2D cross-correlation method with a prior constraint (Palander 2007). If the rotation stability condition does not hold, the object can be still reconstructed using the statistical methods described in Section 3.1, but the computational advantage is lost and the full 3D image alignment (Brandt & Mevorah 2006, Yu et al. 2008) is additionally needed.

It should be noted that the DFBP algorithm can be seen as an spatial interpolation method that resamples projection images from the cylindrical coordinate into the Cartesian coordinate. In Publication 5, the DFBP algorithm has been compared with the bilinear interpolation method and the results showed that, for both the noise-free and the noisy image data, the DFBP method achieves lower error than the linear interpolation for any choices of the number of projections. In principle, the DFBP and the direct spatial interpolation should give similar results, which is in analogy to the FBP and the direct Fourier interpolation. However, in practice the FBP algorithm has become much more popular in computed tomography than the direct Fourier interpolation; one reason for this is that the errors produced by the polar-to-Cartesian interpolation downgrades the performance of the direct interpolation (Stark et al. 1981, Choi & Munson 1998). We may expect the same analogy in the dual setting on the favour of the DFBP method in the micro-rotation application.

As a final note, we believe that the duality concept is important because the duality can be seen in more widespread context: every algorithm, assuming similar projection models, has its dual form applicable in the dual domain, and this motivates the development and dualisation of other existing algorithms. The notion of duality thus suggests a whole collection of new algorithms and

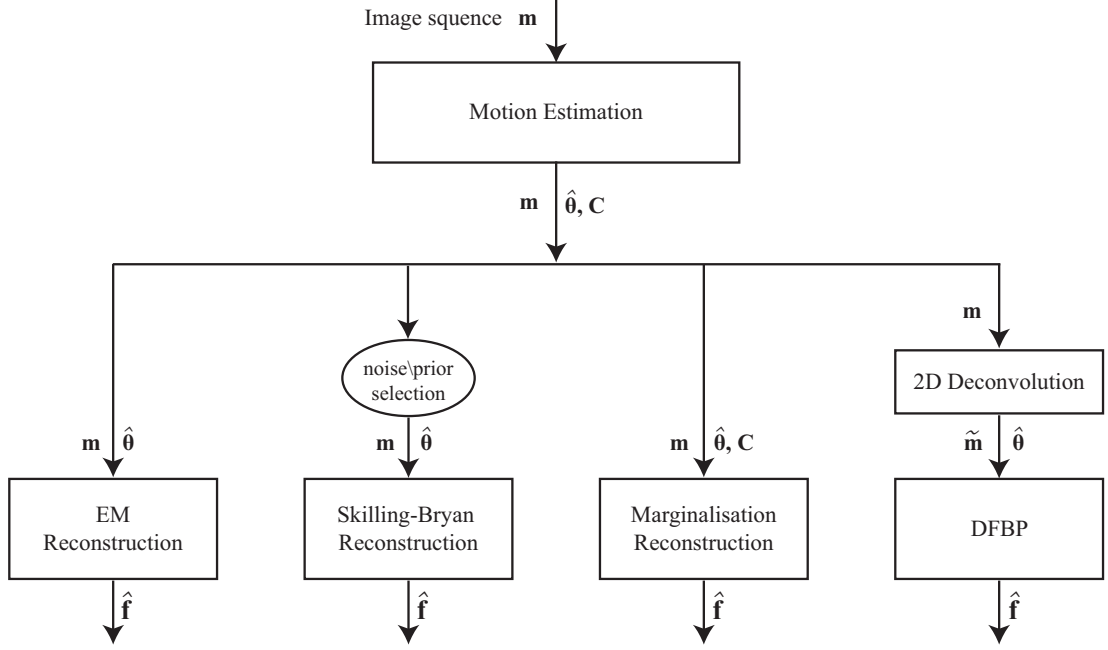


Figure 3.4: Flow chart of the four reconstruction methods for micro-rotation fluorescence imaging.

interpretations to have practical value in the novel micro-rotation application.

3.3 Summary and Examples

This Chapter has considered the methods of expectation maximisation, Skilling-Bryan optimisation, marginalisation and dual filtered backprojection for the 3D structure reconstruction from a series of micro-rotation images. Figure 3.4 shows the flow graph of the proposed reconstruction algorithms. All the algorithms require motion parameters as the input (Figure 3.1). The EM method is a closed-form, iterative algorithm bases on the Poisson noise model and the Skilling-Bryan method is second-order, subspace optimisation enabling the use of more general noise and prior models. The marginalisation method additionally requires the covariance matrix characterising uncertainty in the estimated motion parameters and the DFBP algorithm needs 2D convolution as a preprocessing step. The marginalisation approach is capable to compensate reconstruction artefacts caused by the inaccurate motion estimate at an additional cost in computational complexity, whereas the DFBP approach benefits from the fastest computational speed but it restricts itself with the confocal imaging modality and a good stability of cell rotation. Finally, to give an idea how micro-rotation reconstructions look like, two examples of the reconstruction using the EM algorithm are displayed in Figure 3.5 for a *Caenorhabditis elegans* embryo, and Figure 3.6 for the mitochondria and nuclear envelope of a single human living cell.

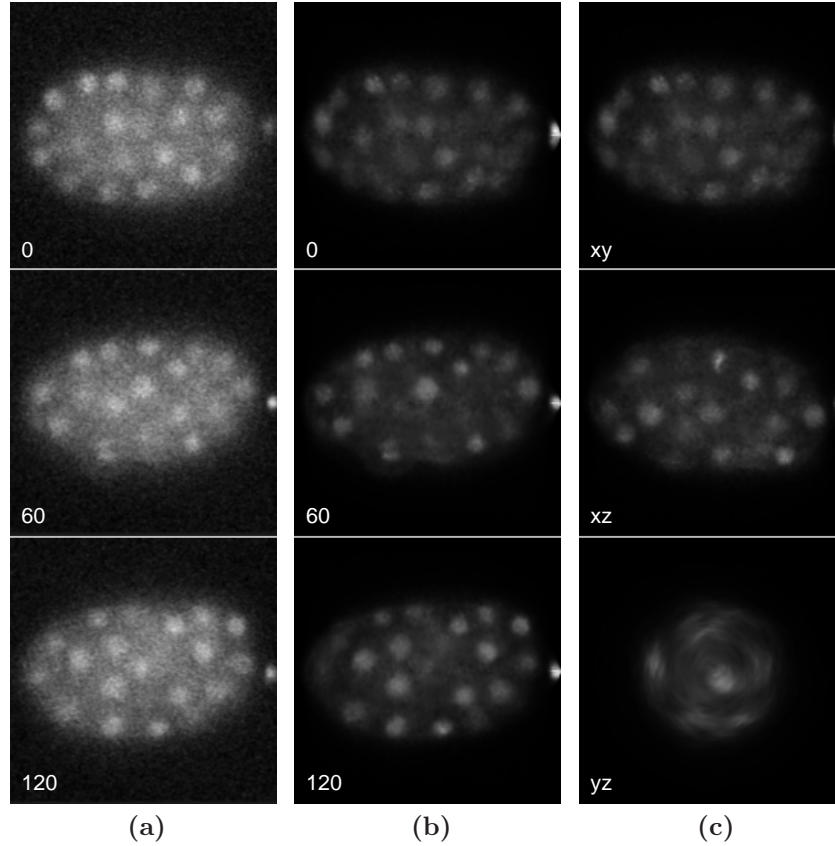


Figure 3.5: Micro-rotation widefield fluorescence images of a *Caenorhabditis elegans* embryo expressing a protein marker (Histone-GFP). The 397 micro-rotation images (pixel size 254×254 nm) were acquired using a $63\times$ water-immersion objective (numerical aperture 1.2) and a widefield microscope (excitation wavelength 488 nm and emission wavelength 520 nm) with the frame rate 32 images/sec. The images were aligned and cropped the region of interest using the correlation method; the final size used was 175×175 pixels and the number of imaged was 65 for a half rotation. (a) Three raw-image example at angle 0° , 60° and 120° ; (b) EMTV reconstruction slices corresponding to slices in (a); (c) EMTV reconstruction showing the xy , xz , yz slices at the volume centre, where the rotation axis is in the horizontal (x) direction, see the acquisition geometry in Figure 2.4c. It is obvious that high-frequency noise appear in the raw images have been removed and the reconstructed object is sharper and higher in contrast; Although the reconstruction on the xy and xz views (parallel to the rotation axis x) is better than that on the yz view (orthogonal to the rotation axis).

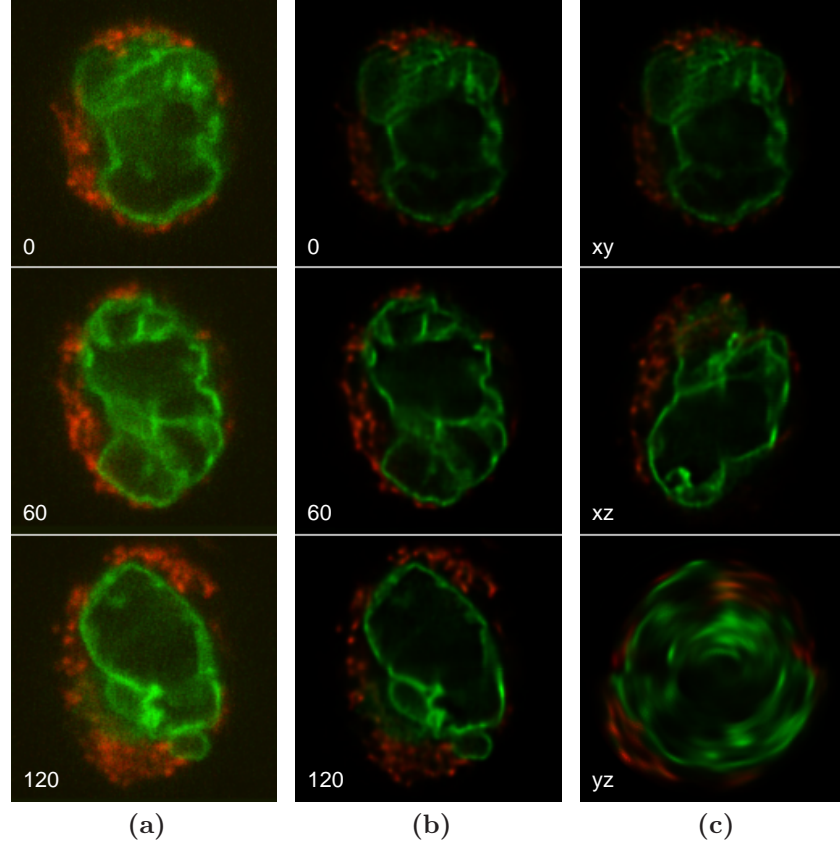


Figure 3.6: Micro-rotation confocal fluorescence images of a single human living cell in suspension. The single cell expresses a nuclear envelope marker (lamin-GFP; green) and stained with a mitochondria marker (mito-OFP; red). The two series (red and green) of micro-rotation images (pixel size 127×127 nm.) were acquired using a $63\times$ water-immersion objective (numerical aperture 1.2) and a spinning-disk confocal microscope (excitation wavelength 488 nm and emission wavelength 520 nm) with the frame rate 8.6 images/sec. . The two images series were aligned and cropped the region of interest using the correlation method; the final size used was 165×165 pixels and the number of imaged was 43 for a half rotation. (a) Three raw-image example; (b) EMTV reconstruction slices corresponding to (a); (c) EMTV reconstruction showing the three orthogonal slices at the volume centre. As the same in Figure 3.5, the result is clearer and sharper with fine details, but the reconstruction on the views parallel to the rotation axis x is better than that on the view orthogonal to the rotation axis, especially along the tangential direction of the rotation.

Chapter 4

Results and Method Assessments

This chapter summarises important results and assessments of the proposed reconstruction methods based on the five Publications. Publication 1-4 are built on the statistical inversion theory described in Section 3.1. Each publication concentrates on different statistical points of view in utilising prior information and modelling uncertainties, arisen from measurement noise, missing data, and image alignment. Publication 5 presents the reconstruction method based on the Fourier inversion which is addressed in Section 3.2.

Publication 1 proposed the Bayesian reconstruction method that assumes Gaussian noise and the Gaussian prior for the posterior distribution (3.1). In this work, we used the MAP method (3.6) for estimating the object density from the posterior distribution and, thereafter, employed the trust-region optimisation method, implemented in MatlabTM (Coleman & Li 1996), for minimising the posterior cost function (3.7). The proposed method was tested with a series of micro-rotation images of prophase chromosomes in cell mitosis (see Table 4.1 for image acquisition details). The results with the real dataset demonstrated that the proposed method is promising for determining the 3D object structure from micro-rotation images.

In Publication 2, we generalised the original Skilling-Bryan method, discussed in Section 3.1.1, for solving the posterior cost function with *general* noise models and object prior functions. As a simulation, the proposed method was tested with 2D simulated data that assume the Gaussian and Poisson noise together with the Gaussian, the entropy and the total variation (TV) priors. The results showed that, for the same prior function, the difference between the reconstructions that assume the Poisson and Gaussian noise appears fairly small, whereas the reconstruction with the TV prior is clearly better than the one with the Gaussian and entropy priors. In term of the convergence of algorithm, we found only minor difference between the three different priors, but the selection of the noise models seems to have higher impact to the algorithm convergence (see Figure 4.1). In addition to the 2D simulation, we reported our 3D simulation of micro-rotation imaging with a 3D simulated cell, where the results showed that the generalised

	Publication 1	Publication 3	Publication 4&5
Object types	chromosomes in cell mitosis	nuclear envelope in human cell	nuclear envelope in human cell
Imaging modes	widefield	widefield	spinning-disk confocal
Pixel size (nm)	129×129	127×127	127×127
Image size (pixels)	195×212	295×298	400×400
Number of images	90	378	175
Fundamental period	18.1	143	82
Recon. size (pixels)	$121 \times 121 \times 121$	$150 \times 150 \times 150$	$155 \times 155 \times 155$

Table 4.1: Image acquisition details of real micro-rotation datasets used in the described publications.

Skilling-Bryan method is capable of solving the wide class of measurement noise and prior model.

Publication 3 proposed to solve the reconstruction problem by using the expectation maximisation method with the TV object prior, or the EMTV method which has been addressed in Section 3.1.2. In this work, we first reported our 3D simulation on a 3D phantom object to evaluate the properties of the proposed method and to compare micro-rotation imaging with through-stack imaging protocol. The simulation illustrated in Figure 4 of Publication 3 showed that, for through-stack imaging, the resulting reconstruction contains high resolution details in the lateral planes (xy), but some blur remains in the axial planes (xz , yz), particularly along the optical axis (z); On the other hand, for micro-rotation imaging, the reconstruction is sharp on the planes parallel to the rotation axis (x -axis), but it is blurred in the planes (xy , xz) orthogonal to the rotation axis, especially in the tangential direction of the rotation. More precisely, through-stack imaging suffers from poor axial z resolution whereas micro-rotation imaging gives weak tangential resolution on the directions orthogonal to the rotation axis. Furthermore, we compared the proposed EMTV method (3.14) to the standard EM method (3.13) as well as the EM method with the spatial-derivative prior (EMGR) suggested by Green (1990). The results showed that the reconstructions with the EMTV and the EMGR are clearly better than the one with the EM approach, whereas the difference in the quality of the reconstruction between the EMTV and the EMGR is fairly small. Finally, the proposed method was tested with real micro-rotation images of a human living cell expressing a fluorescent nuclear-envelope marker (Table 4.1). The experiment demonstrated that the proposed method was successful with the real dataset although the rotation geometry leads to some artefacts visible on the planes parallel to the yz -plane, which is similar to the results reported in the simulation.

Publication 4 presented a Bayesian marginalisation method, described in Section 3.1.3, for determining 3D object structure from a micro-rotation image series

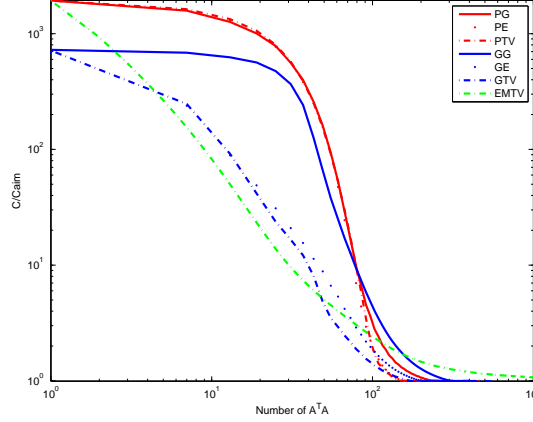


Figure 4.1: Convergence curves of the six reconstructions using the generalised Skilling–Bryan method that assumes Gaussian and Poisson noise together with the Gaussian, the entropy and the total variation prior functions. The actual reconstructions correspond to the results presented in Figure 2 of Publication 2.

in consideration with uncertainty in the motion estimates. We first evaluated the proposed method by a 2D simulation with the Shepp-Logan 2D head phantom. The reconstructions of the head phantom were estimated using the marginalisation method and the standard MAP method with the correct and incorrect (perturbed) motion parameters. The simulation results showed that the marginalisation method gives visually and numerically better results than the standard MAP method for any degrees of uncertainty in the motion estimates. Moreover, we tested the proposed method with a real micro-rotation set which represents the nuclear membrane of a single human living cell, expressed by green fluorescent markers (Table 4.1). The 3D reconstructions of the cell were computed using the standard MAP and the marginalisation algorithm with the initial and estimated motion parameters. The results from the real dataset showed that the reconstruction with the standard MAP clearly contains smearing artefacts in all directions whereas the marginalisation approach smooths out the motion-uncertainty artefacts appearing on the object structure. However, when the motion parameters have been accurately recovered, the marginalisation method provides only minor improvement comparing with the standard MAP estimate.

Publication 5 suggested the dual filtered backprojection (DFBP) algorithm for solving 3D reconstructions from micro-rotation images acquired by a confocal microscope. As the first proof of the DFBP principle, we reconstructed the 2D Shepp Logan phantom from 1D projections and compared the DFBP method to the direct spatial linear interpolation where deconvoluted data is merely resampled from the cylindrical coordinate frame into the Cartesian coordinate system. The results showed that, for both the noise-free and noisy phantoms, the DFBP method achieves lower error than the standard linear interpolation for any choice of number of projections. Furthermore, we computed the 3D reconstruction of

the simulated cell by the DFBP method and compared it to the linear interpolation. The reconstruction results demonstrated that both DFBP and the alternative interpolation method produced good results. Finally, we experimented the proposed method with the real micro-rotation confocal dataset used in Publication 4, and also compared the DFBP method with the linear interpolation and the EMTV method presented in Publication 3. The reconstruction obtained with the DFBP is slightly better than the one with the linear interpolation method, whereas the EMTV reconstruction appears clearly sharper than those of the two reconstructions. The EMTV method however needs more computational effort due to the required, repetitive computation of the 3D-2D transformations between object and images.

As we have seen in all the Publications, micro-rotation reconstruction always contains poor resolution in the tangential direction on the view orthogonal to the rotation axis, regardless of reconstruction methods we applied. The tangential resolution limitation is due to the fact that the elongation of PSF orients to the direction orthogonal to the image plane, which is the tangential direction of the rotation in the micro-rotation setting. One possibility to improve the tangential resolution is to use the micro-rotation imaging protocol with extended depth-of-focus (EDF) microscopes (Arnison et al. 2003, Botcherby et al. 2006, Wicker & Heintzmann 2007). The attractive feature of the EDF microscopes is that it greatly enlarges the depth-of-focus of the microscope, while the lateral resolution is still preserved. In this way, the image formation model of the combined micro-rotation imaging with the EDF microscope is close to the straight-line projection in classical computed tomography, or X-ray tomography (Kak & Slaney 1988). An explanation for the concept how the tangential resolution can be improved by EDF microscopy is illustrated in Figure 4.2. To evaluate this concept, we made a 2D simulation that compares the micro-rotation reconstructions using a wide-field PSF and a depth-of-focus PSF. Figure 4.3 shows that, for the conventional PSF, the weakness in tangential direction remains unsolved when the number of projections increases; By contrast, the tangential resolution is clearly enhanced for the extended-focus PSF with increasing the number of projections.

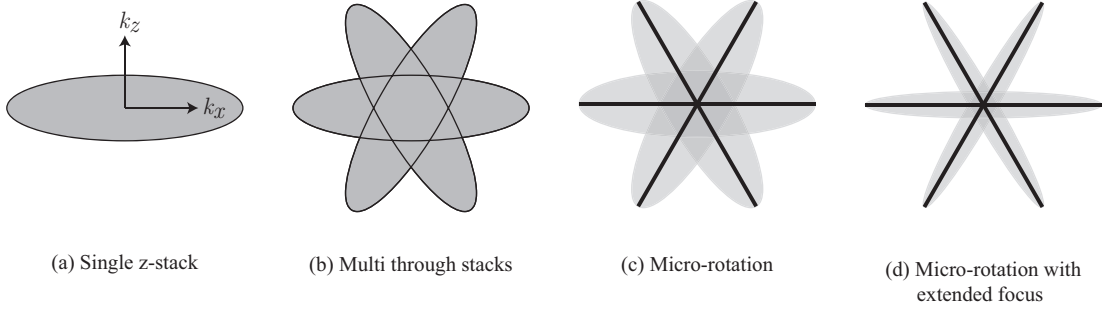


Figure 4.2: Comparison of the frequency support between four different imaging geometries. (a) Single through-stack imaging gives the limited frequency support (ellipse) of PSF in the z direction that leads band-limited resolution in the z -axis (k_x and k_z denote the spatial frequency in the x and z directions); (b) Multiple through-stack imaging enlarges the frequency support along the z -axis by collecting multiple image stacks in different orientations; (c) Micro-rotation imaging projects the frequency support (each ellipse) to its central line in the orthogonal direction. As a consequence, the orthogonal projection of the frequency support is the major cause of optical blur in the tangential direction of the rotation; (d) Micro-rotation imaging with extended depth-of-focus microscope narrows each ellipse approximately closer to the central line and, therefore, the resolution improvement in the tangential direction can be achieved.

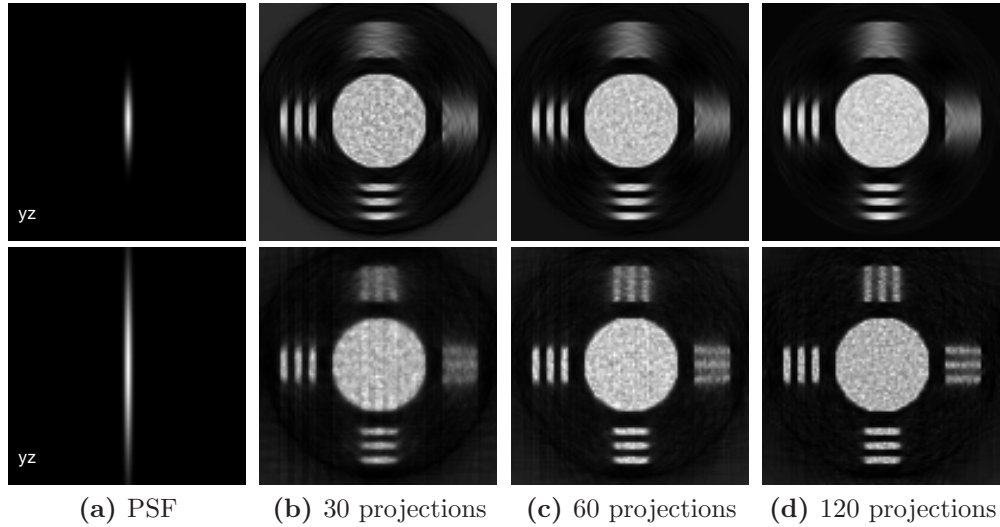


Figure 4.3: 2D simulation of micro-rotation reconstruction with (upper row) conventional and (lower row) extended-focus point spread function (PSF). (a) conventional PSF (upper) and extended-focus PSF (lower) with the anisotropic Gaussian kernel; (b–d) reconstructions from different number of 1D projections: 30, 60 and 120, respectively. The true test phantom refers to Figure 1 in Publication 2.

Chapter 5

Conclusions and Discussion

This thesis has presented four different methods for estimating 3D object structures from a series of micro-rotation images, assuming that the motion parameters are available. The developed methods include the generalised Skilling-Bryan method, the expectation maximisation with total variation (EMTV) method, the Bayesian marginalisation method and the dual filtered backprojection (DFBP) method. The three former approaches are built on a valid statistical framework that allows a straightforward utilisation of prior knowledge and modelling various kinds of uncertainty. The last approach is based on the direct Fourier inversion which is derived from the observed duality of the classical filtered backprojection (FBP) algorithm. The key features of the reconstruction methods are summarised as follows:

- The EMTV algorithm is an efficient tool for determining object density for both widefield and confocal microscopy. An attraction of this algorithm is that it provides a closed-form iterative solution with the built-in nonnegativity constraint, although the algorithm is slow in convergence particularly in the latter iterations. The processing time of the EMTV algorithm can be measured in tens of minutes for the reconstruction size of $100 \times 100 \times 100$ pixels.
- The generalised Skilling-Bryan method can be used to reconstruct object density assuming a wide class of measurement noise and object prior knowledge. As a common characteristic of second-order optimisation, the Skilling-Bryan method is slow in convergence during the former iterations but superior in the latter iterations. The hybrid approach that first uses the EMTV algorithm and follows by the Skilling-Bryan method, can be used to speed up the algorithm convergence. The computational time of the generalised Skilling-Bryan method is in hours.
- The Bayesian marginalisation method can be used to improve the object reconstruction which suffers from artefacts introduced by the inaccurate

motion estimates. This method however requires extra computations and gives only minor improvement when the motion parameters are accurately recovered. The computing time of this method can be up to tens of hours.

- The DFBP algorithm is a fast and robust method for reconstructing object from a micro-rotation image series, acquired by a confocal microscope. The DFBP is attractive for solving the reconstruction problem since it provides equivalent features to the FBP method including fast computation and good-quality reconstruction for projections with complete angular coverage. The computing time of the DFBP method can be measured in minutes.

An important result in the modelling of measurement noise and object priors is that the resulting reconstruction that assumes the Gaussian noise model differs slightly from the reconstruction assuming the Poisson model. However, the selection of object prior is far more important than that of the noise model. The spatial-derivative priors, such as the TV and the Green's prior functions, give clearer and sharper structures than the Gaussian and the entropy priors, independent of noise models we select; but the difference in reconstruction quality between the Gaussian and the entropy priors appears fairly small. Further interesting research in prior modelling should be thus emphasised on the investigation and comparison of various definitions of spatial-derivative prior proposed by many authors (Verveer et al. 1999, Dey et al. 2006, Vicidomini et al. 2006).

Another essential finding in the micro-rotation technique is its unique imaging characteristic. That is, the 3D optical resolution of micro-rotation imaging is highly bounded in the tangential directions appeared on the yz planes (that are orthogonal to the rotation x axis), in contrast to the through-stack imaging that has bounded resolution in the axial z direction. The resolution limit of both imaging protocols arises from the same reason: according to the elongation of PSF in the z -axis, resolution in the direction orthogonal to the image plane is always worse than that in the direction parallel to the focal plane. In through-stack imaging, most of the researchers have focused to improve the axial resolution by decreasing the depth-of-focus using various sophisticated high-resolution techniques (Gustafsson 1999). However, in micro-rotation imaging, the limited tangential resolution can be enhanced by enlarging the depth-of-focus using extended depth-of-focus microscopy (see, for instance, Arnison et al. 2003, Botcherby et al. 2006). Moreover, increasing the depth-of-focus in micro-rotation imaging not only improves the tangential resolution, but also helps the motion estimation in a way that the z translation can be ignored and the motion estimation methods become more powerful due to the better appearance of features on projection images.

In conclusion, the methods proposed in the thesis have been demonstrated as useful tools for solving object reconstruction in the micro-rotation imaging application. A nice aspect of this thesis is that the proposed methods are presented in a formalism that allows straightforward extension of the ideas to other existing imaging applications in inverse problems.

Bibliography

- Abbott, A. (2003), ‘Cell culture: Biology’s new dimension’, *Nature* **424**, 870–872.
- Agard, D. A., Hiraoka, Y., Shaw, P. J. & Sedat, J. W. (1989), ‘Fluorescence microscopy in three dimensions’, *Methods Cell Biol* **30**, 353–377.
- Anconelli, B., Bertero, M., Boccacci, P., Desiderà, G., Carbillet, M. & Lanteri, H. (2006), ‘Deconvolution of multiple images with high dynamic range and an application to LBT LINC-NIRVANA’, *Astronomy and Astrophysics* **460**, 349–355.
- Arnison, M., Cogswell, C., Sheppard, C. & Török, P. (2003), Wavefront coding fluorescence microscopy using high aperture lenses, *in* F. Kao & P. Török, eds, ‘Optical Imaging and Microscopy’, Springer, pp. 143–165.
- Biggs, D. S. C. (2004), ‘Clearing up deconvolution’, *Biophotonics Int.* **11**, 32–36.
- Born, M. & Wolf, E. (1999), *Principles of optics*, 7th edn, Cambridge University Press, London.
- Botcherby, E., Juskaitis, R. & Wilson, T. (2006), ‘Scanning two photon fluorescence microscopy with extended depth of field’, *Optics Communications* **268(2)**, 253–260.
- Bradl, J., Rinke, B., Schneider, B., Edelmann, P., Krieger, H., Hausmann, H. & Cremer, C. (1996), ‘Resolution improvement in 3-D microscopy by object tilting’, *Microsc. Anal.* **44**, 99–11.
- Brandt, S. S. & Kolehmainen, V. (2007), ‘Structure-from-motion without correspondence from tomographic projections by Bayesian inversion theory’, *IEEE Transactions on Medical Imaging* **26**, 238–248.
- Brandt, S. S. & Mevorah, M. (2006), Camera motion recovery without correspondence from micro-rotation sets in wide-field light microscopy, *in* ‘Proc. Statistical Methods in Multi-Image and Video Processing Workshop, in conjunction with ECCV 2006’, Graz, Austria.

- Byrne, C. L. (1998), ‘Accelerating the emml algorithm and related iterative algorithms by rescaled block-iterative methods’, *Trans. Image Process.* **7**, 100–109.
- Calvetti, D. & Somersalo, E. (2007), *Intorduction to Bayesian Scientific Computing - Ten Lectures on Subjective Computing*, Vol. 2 of *Surveys and Tutorials in the applied Mathematical Sciences*, Springer Verlag, New York.
- Carrington, W. A. (1990), ‘Image restoration in 3D microscopy with limited data’, *Proc. SPIE* **1205**, 72–83.
- Carrington, W. A., Lynch, R. M., Moore, E. D., Isenberg, G., Fogarty, K. E. & Fay, F. S. (1995), ‘Superresolution three-dimensional images of fluorescence in cells with minimal light exposure’, *Science* **268**, 1483–1487.
- Choi, H. & Munson, D. C. (1998), ‘Direct-Fourier reconstruction in tomography and synthetic aperture radar’, *International Journal of Imaging Systems and Technology* **9**(1), 1–13.
- Cogswell, C. J., Larkin, K. G. & Klemm, H. U. (1996), ‘Fluorescence microtomography: multi-angle image acquisition and 3D digital reconstruction’, *Proc. SPIE* **2655**, 109–115.
- Coleman, T. & Li, Y. (1996), ‘An interior, trust region approach for nonlinear minimisation subject to bounds’, *SIAM J. Optim.* **6**, 418–445.
- Conchello, J. A. (1998), ‘Superresolution and convergence properties of the expectation-maximization algorithm for maximum-likelihood deconvolution of incoherent images’, *J. Opt. Soc. Am. A* **15**, 2609–2619.
- Conchello, J. & McNally, J. (1996), ‘Fast regularization technique for expectation maximization algorithm for optical sectioning microscopy in three-dimensional microscopy’, *Proc. SPIE* **2655**, 199–208.
- Csiszár, I. (1991), ‘Why least squares and maximum entropy? An axiomatic approach to inference for linear inverse problems’, *Ann. Stat.* **19**, 2032–2066.
- Dempster, A., Laird, N. & Rubin, D. (1977), ‘Maximum likelihood from incomplete data via the EM algorithm’, *Journal of the Royal Statistical Society Series B* **39**, 1–38.
- den Dekker, A. J. & van den Bos, A. (1997), ‘Resolution: a survey’, *J. Opt. Soc. Am. A* **14**, 547–557.
- Dey, N., Blanc-Féraud, L., Zimmer, C., Kam, Z., Roux, P., Olivo-Marin, J. & Zerubia, J. (2006), ‘Richardson-Lucy algorithm with total variation regularization for 3D confocal microscope deconvolution’, *Microscopy Research Technique* **69**, 260–266.

- Engelhardt, P. (2000), Electron tomography of chromosome structure, *in* R. A. Meyers, ed., 'Encyclopaedia of Analytical Chemistry', Vol. 6, Chichester Wiley, New York.
- Erhardt, A., Zinser, G., Komitowski, D. & Bille, J. (1958), 'Reconstructing 3-d light-microscopic images by digital image processing', *Appl. Opt.* **24**, 194–200.
- Fish, D. A., Brinicombe, A. M., Pike, E. R. & Walker, J. G. (1995), 'Blind deconvolution by means of the Richardson-Lucy algorithm', *J. Opt. Soc. Am. A* **12**, 58–65.
- Frank, J. (2006), *Three-Dimensional Electron Microscopy of Macromolecular Assemblies*, 2 edn, Oxford University Press, New York.
- Frank, J. & McEwen, B. F. (1992), Alignment by cross-correlation, *in* J. Frank, ed., 'Electron Tomography; Three Dimensional Imaging with the Transmission Electron Microscope', Plenum Press, New York, USA, chapter 9, pp. 205–213.
- Fuhr, G., Müller, T., Schnelle, T., Hagedorn, R., Voigt, A., Fiedler, S., Arnold, W. M., Zimmermann, U., Wagner, B. & Heuberger, A. (1994), 'Radio-frequency microtools for particle and live cell manipulation', *Naturwissenschaften* **81**, 528–535.
- Galatsanos, N. & Katsaggelos, A. (1992), 'Methods for choosing the regularization parameter and estimating the noise variance in image restoration and their relation', *IEEE Trans. on Image Processing* **1**, 322–336.
- Gibson, S. F. & Lanni, F. (1991), 'Experimental test of an analytic model of aberration in an oil-immersion objective lens used in 3D light microscopy', *J. Opt. Soc. Am A* **8**, 1601–1613.
- Goodman, J. (2005), *Introduction to Fourier Optics*, 3 edn, Springer, Roberts and Company.
- Green, P. J. (1990), 'Bayesian reconstructions from emission tomography data using a modified EM algorithm', *IEEE. Transactions on Medical Imaging* **9**, 84–93.
- Gull, S. & Skilling, J. (1999), 'Quantified maximum entropy', *MemSys5 User's Manual, V.1.2*.
- Gustafsson, M. (1999), 'Extended resolution fluorescence microscopy', *Curr Opin Struct Biol* **9**(5), 627–634.

- Gustafsson, M., Shao, L., Carlton, P., Wang, C., Golubovskaya, I., Cande, W., Agard, D. & Sedat, J. (2008), 'Three-dimensional resolution doubling in wide-field fluorescence microscopy by structured illumination.', *Biophys J.* **94**(12), 4957–4970.
- Heintzmann, R. & Cremer, C. (2002), 'Axial tomographic confocal fluorescence microscopy', *Journal of Microscopy* **206**, 7–23.
- Hell, S. & Stelzer, E. (1992), 'Properties of a 4pi confocal fluorescence microscope', *J. Opt. Soc. Am.* **9**, 2159–2166.
- Hell, S. W. (2009), 'Microscopy and its focal switch', *Nature Methods* **1**, 24–32.
- Holmes, T. J. (1989), 'Expectation-maximization restoration of band-limited, truncated point-process intensities with application in microscopy', *Journal of the Optical Society of America A* **6**(7), 1006–1014.
- Holmes, T. J. (1992), 'Blind deconvolution of quantum-limited incoherent imagery maximum-likelihood approach', *J. Opt. Soc. Am. A* **9**, 1052–1062.
- Holmes, T. J., Biggs, D. & Abu-Tarif, A. (2006), Blind deconvolution, in J. B. Pawley, ed., 'Handbook of Biological Confocal Microscopy', 3 edn, Springer, New York.
- Hudson, H. M. & Larkin, R. S. (1994), 'Accelerated image reconstruction using ordered subsets of projection data', *IEEE Trans. Med. Imaging* **13**, 601–609.
- Huisken, J., Swoger, J. & Stelzer, E. H. (2007), 'Three-dimensional optical manipulation using four collimated intersecting laser beams', *Optics Express* **8**, 4921–4928.
- Jain, A. K. (1989), *Fundamentals of Digital Image Processing*, Prentice Hall.
- Jannetta, A., Jackson, J. C., Kotre, C. J., Birch, I. P., Robson, K. J. & Padgett, R. (2004), 'Mammographic image restoration using maximum entropy deconvolution', *Phys. Med. Biol.* **49**, 4997–5010.
- Jaynes, E. (2003), *Probability Theory: The Logic of Science*, Cambridge University Press.
- Kaipio, J. & Somersalo, E. (2004), *Statistical and Computational Inverse Problems*, Springer, Berlin.
- Kak, A. C. & Slaney, M. (1988), *Principles of Computerized Tomographic Imaging*, IEEE Press.

- Kang, H., Jenabi, J., Zhang, J., Keshelava, N., Shimada, H., May, W., Ng, T., Reynolds, C., Triche, T. & Sorensen, P. H. (2007), 'E-cadherin cell-cell adhesion in ewing tumor cells mediates suppression of anoikis through activation of the erbb4 tyrosine kinase', *Cancer Res.* **67**(7), 3094–3105.
- Karr, A. F. (1993), *Probability*, Springer, New York.
- Kolehmainen, V., Siltanen, S., Järvenpää, S., Kaipio, J., Koistinen, P., Lassas, M., Pirttilä, J. & Somersalo, E. (2003), 'Statistical inversion for medical x-ray tomography with few radiographs ii: Application to dental radiology', *Phy. Med. Bio.* **48**, 1465–1490.
- Korlach, J., Reichle, C., Müller, T., Schnelle, T. & Web, W. W. (2005), 'Trapping, deformation, and rotation of giant unilamellar vesicles in octode dielectrophoretic field cage', *Biophysical Journal* **89**, 554–562.
- Larson, J. M. (2002), '2D and 3D deconvolution of confocal fluorescence images by maximum likelihood estimation', *Proc. SPIE* **4621**, 86–94.
- Lee, M., Ko, S., Kim, H., Kim, Y., Lee, S., Kim, S., Jong, H., Kim, T., Lee, J. & Bang, Y. (2004), 'Smad2 mediates erk1/2 activation by tgf-beta1 in suspended, but not in adherent, gastric c', *Int. J. Oncol.* **24**, 1229–34.
- Lizundia, R., Sengmanivong, L., Guernon, J., Müller, T., Schnelle, T., Langsley, G. & Shorte, S. L. (2005), 'Using micro-rotation imaging to study jnk-mediated cell survival in theileria parva-infected b-lymphocytes', *Parasitology* **130**, 1–7.
- Lucy, L. B. (1974), 'An iterative technique for the rectification of observed distributions', *Astron. J.* **79**, 745–754.
- Markham, J. & Conchello, J. (2001), 'Fast maximum-likelihood image-restoration algorithms for three-dimensional fluorescence microscopy', *J. Opt. Soc. Am. A* **18**(5), 1062–1071.
- McLachlan, G. & Krishnan, T. (2008), *The EM Algorithm and Extensions*, 2 edn, Wiley Interscience, USA.
- McNally, J. G., Karpova, T., Cooper, J. & Conchello, J. (1999), 'Three-dimensional imaging by deconvolution microscopy', *Methods* **19**, 373–385.
- Murphy, D. B. (2001), *Fundamentals of Light Microscopy and Electronic Imaging*, John Wiley and Sons, New York.
- Nocedal, J. & Wright, S. (2006), *Numerical Optimization*, 2 edn, Springer Verlag.
- Novotny, L. & Hecht, B. (2006), *Principles of nano-optics*, Cambridge University Press, New York.

- Palander, K. (2007), Camera motion estimation in micro-rotation imaging, Master's thesis, Helsinki University of Technology.
- Pawley, J. B. (2006), *Handbook of Biological Confocal Microscopy*, 3 edn, Springer.
- Pickup, L. C., Capel, D. P., Roberts¹, S. J. & Zisserman, A. (2007), 'Bayesian methods for image super-resolution', *The Computer Journal* pp. bxm091+.
- Pytlak, R. (1998), 'An efficient algorithm for large-scale nonlinear programming problems with simple bounds on the variables', *SIAM J. Optim* **8**, 532–560.
- Renaud, O., Vina, J., Yu, Y., Machu, C., Trouvé, A., der Voort, H. V., Chalmond, B. & Shorte, S. L. (2008), 'High-resolution 3-d imaging of living cells in suspension using confocal axial tomography', *Biotechnol J.* **3**(1), 53–62.
- Richardson, H. W. (1972), 'Bayesian-based iterative method of image restoration', *J. Opt. Soc. Am.* **62**, 55–59.
- Schnelle, T., Hagedorn, R., Fuhr, G., Fiedler, S. & Müller, T. (1993), 'Three-dimensional electric field traps for manipulation of cells—calculation and experimental verification', *Biochim. Biophys. Acta.* **1157**, 127–140.
- Schnelle, T., Müller, T., Gradl, G., Shirley, S. G. & Fuhr, G. (2000), 'Dielectrophoretic manipulation of suspended submicron particles', *Electrophoresis* **21**, 66–73.
- Shaw, P. J., Agard, D. A., Hiraoka, Y. & Sedat, J. W. (1989), 'Tilted view reconstruction in optical microscopy. Three-dimensional reconstruction of drosophila melanogaster embryo nuclei', *Biophysical Journal* **55**, 101–110.
- Shepp, L. A. & Vardi, Y. (1982), 'Maximum likelihood reconstruction in positron emission tomography', *IEEE Trans. Medical Imaging* **1**, 113–122.
- Shorte, S. L., Muller, T. & Schnelle, T. (2003), 'Method and device for 3 dimensional imaging of suspended micro-objects providing high-resolution microscopy', Patent. Patent Number; EP 02 292 658.8; file date: 25 October 2002.
- Skilling, J. (1989), Classic maximum entropy, in J. Skilling, ed., 'Maximum Entropy and Bayesian Methods', Kluwer Academic.
- Skilling, J. & Bryan, R. K. (1984), 'Maximum entropy image reconstruction: general algorithm', *Mon. Notices R. Astron. Soc.* **211**, 111–124.
- Sotthivirat, S. & Fessler, J. (2003), 'Relaxed ordered-subset algorithm for penalized-likelihood image restoration', *J Opt Soc Am A* **20**(3), 439–449.

- Stark, H., Woods, J., Paul, I. & Hingorani, R. (1981), 'An investigation of computerized tomography by direct Fourier inversion and optimum interpolation', *IEEE Trans. Biomed. Eng* **28**(7), 496–505.
- Thompson, A. M. (1988), On the use of quadratic regularisation within maximum entropy image restoration, in J. Skilling, ed., 'Maximum Entropy and Bayesian Methods', Kluwer Academic Publishers, pp. 497–504.
- Tipping, M. E. & Bishop, C. (2003), 'Bayesian image super-resolution', *Advances in Neural Information Processing Systems* **15**, 1279–1286.
- Török, P. & Kao, F.-J. (2003), *Optical imaging and microscopy: techniques and advanced systems*, Springer Press, New York.
- Triggs, B., McLauchlan, P., Hartley, R. & Fitzgibbon, A. (2000), Bundle adjustment – a modern synthesis, in B. Triggs, A. Zisserman & R. Szeliski, eds, 'Vision Algorithms: Theory and Practice', Vol. 1883 of *LNCS*, Springer-Verlag, Berlin/New York, pp. 298–372.
- van der Voort, H. & Strasters, K. (1995), 'Restoration of confocal images for quantitative image analysis', *Journal of Microscopy* **178**, 165–181.
- van der Voort, H. T. M. & Brakenhoff, G. J. (1990), '3D-image formation in high aperture fluorescence confocal microscopy', *J. Microsc.* **158**, 43–54.
- van Kempen, G. M. P., van Vliet, L. J., Verveer, P. J. & van der Voort, H. T. M. (1997), 'A quantitative comparison of image restoration methods for confocal microscopy', *Journal of Microscopy* **185**, 354–365.
- van Kempen, G. & van Vliet, L. (1999), 'The influence of the background estimation on the superresolution properties of non-linear image restoration algorithms', *Journal of Microscopy* **198**, 63–75.
- Verveer, P. J., Gemkow, M. J. & Jovin, T. M. (1999), 'A comparison of image restoration approaches applied to three-dimensional confocal and wide-field fluorescence microscopy', *Journal of Microscopy* **193**, 50–61.
- Verveer, P. J. & Jovin, T. M. (1997a), 'Acceleration of the ictm image restoration algorithm', *J. Microsc.* **188**, 191–195.
- Verveer, P. J. & Jovin, T. M. (1997b), 'Efficient superresolution restoration algorithms using maximum a posteriori estimations with application to fluorescence microscopy', *J. Opt. Soc. Am. A* **14**, 1696–1706.
- Verveer, P. J. & Jovin, T. M. (1999), 'Improved restoration from multiple images of a single object: Application to fluorescence microscopy', *Applied Optics* **37**, 6240–6246.

- Vicidomini, G., Mondal, P. P. & Diaspro, A. (2006), ‘Fuzzy logic and maximum a-posteriori based image restoration for confocal microscopy’, *Optics Letters* **31(24)**, 3582–3584.
- Webb, D. J. & Horwitz, A. F. (2003), ‘New dimensions in cell migration’, *Nat. Cell Biol.* **5**, 690–692.
- Weir, I. S. (1997), ‘Fully bayesian reconstruction from single photon emission computed tomography data’, *J. Amer. Statist.* **92(437)**, 49–60.
- Wicker, K. & Heintzmann, R. (2007), ‘Interferometric resolution improvement for confocal microscopes’, *Opt. Express* **15**, 12206–12216.
- Yu, Y., Trouvé, A., Wang, J. & Chalmoud, B. (2008), ‘An integrated statistical approach for volume reconstruction from unregistered sequential slices’, *Inverse Problems* **24(4)**, 045004.
- Zipfel, W., Williams, R. & Webb, W. (2003), ‘Nonlinear magic: multiphoton microscopy in the biosciences’, *Nat Biotechnol* **21**, 1369–1377.

ISBN 978-951-22-9754-2 (printed)
ISBN 978-951-22-9755-9 (PDF)
ISSN 1797-3996